Journal of Sustainable Metallurgy
https://doi.org/10.1007/s40831-026-01663-0

RESEARCH ARTICLE

Numerical Investigation of Thermo-reactive Multiphase Flow in a Tuyere-Blown Slag-Fuming Furnace: Part I

Mehrdad Mesgarpour[1] · Andreas Lennartsson[2] · Magnus Ek[3] · Esin İplik[4] · Konstantinos G. Kyprianidis[1] · Rebei Bel Fdhila[1,5]

Received: 23 May 2026 / Accepted: 17 August 2026
© The Author(s) 2026

Abstract

Zinc recovery in a slag-fuming furnace (SFF) is a reduction-smelting process in which coal injected through submerged tuyeres undergoes partial combustion, supplying heat to the bath while generating CO for the reduction of dissolved ZnO and iron oxides. This study examines the metallurgical behavior of an industrial FeO_x–SiO_2–CaO–Al_2O_3–ZnO slag containing 38.5 wt% Fe_2O_3, 21.2 wt% SiO_2, and 6.3 wt% ZnO using a transient two-dimensional Eulerian–Eulerian computational fluid dynamics (CFD) framework. The model couples multiphase flow, finite-rate coal combustion, gas-phase species transport, and slag-reduction reactions with a population balance model that accounts for bubble breakup, coalescence, and the resulting evolution of bubble size and gas–slag interfacial area. Reaction heat enters through a single unified source term. Radiative transfer near the free surface uses a gray-gas model. Slag density, viscosity, and surface tension follow the local temperature and the evolving composition; heat capacity and thermal conductivity follow temperature alone. The reaction mechanism couples the exothermic partial combustion of coal and oxidation of CO with the endothermic reduction of ZnO. Two supporting analyses are reported. In a property-level benchmark against published viscosity measurements for an industrial zinc–copper smelting slag, including the compositional dependence of the viscosity closure reduces the maximum absolute deviation from 47.1 to 22.2% and the mean absolute percentage error from 20.6 to 15.0%, used to select and adjust the closure, so the improvement is not cross-validated against a held-out slag. In a separate parametric sweep, in which the initial bath temperature was varied at fixed injection conditions, the normalized tuyere jet penetration increases from $y/Y = 0.15$ to 0.53 ($y/d_t = 2.5$ to 8.8 on the tuyere-diameter scale) through the temperature dependence of the viscosity closure. The transient calculation predicts a 32.7% concentration-based ZnO depletion over the cycle. The interval of fastest ZnO removal corresponds to the period of highest predicted reduction activity. Within the model, the zinc-fuming rate is therefore controlled by the coupled local availability of CO, gas–slag interfacial area, bubble dynamics, and slag-side mass transfer rather than by equilibrium thermodynamics alone.

The contributing editor for this article was U. Pal.

✉ Mehrdad Mesgarpour
mehrdad.mesgarpour@mdu.se

[1] Mälardalen University, Box 883, 721 23 Västerås, Sweden

[2] Division of Minerals and Metallurgical Engineering, Luleå University of Technology, 971 87 Luleå, Sweden

[3] Boliden Smelters, Boliden AB, Klarabergsviadukten 90, 101 20 Stockholm, Sweden

[4] Linde Sverige AB, Varuvägen 2, 125 30 Älvsjö, Sweden

[5] Hitachi Energy Research, Forskargränd 7, 721 78 Västerås, Sweden

Published online: 22 October 2026

Graphical Abstract

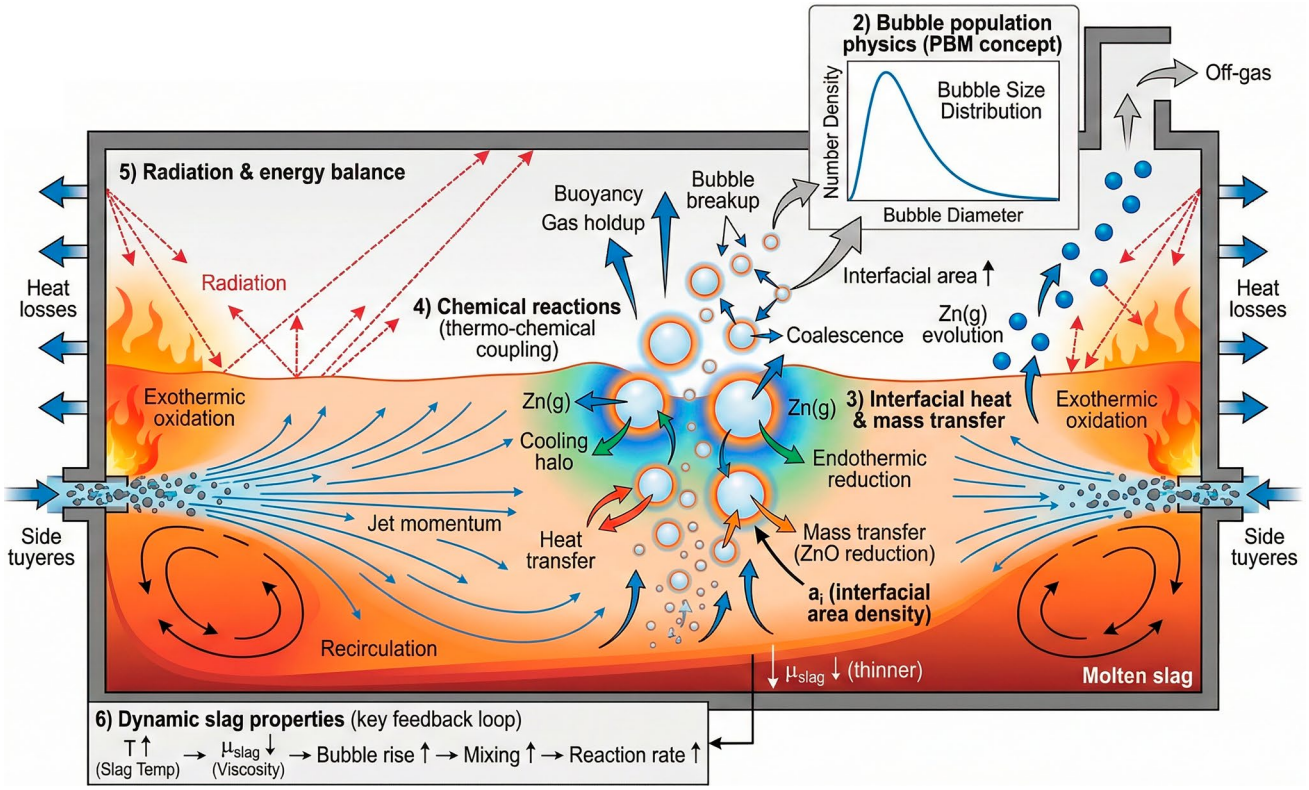

Keywords Reacting multiphase flow · Slag-fuming furnace · Zinc reduction · Slag viscosity · Reaction–heat coupling · Population balance model

Introduction

Copper smelting slag retains several percent zinc and lead after tapping. Fuming under reducing conditions volatilises part of this metal content and conditions the residual slag for reuse or disposal. Its economic viability depends on the feed, the recovery achieved, and the energy and treatment costs, weighed against the downstream product specification. Slag fuming is one such downstream treatment, in which reducing conditions promote the transfer of zinc from the molten slag to the gas phase. It should be distinguished from flash smelting, which treats concentrate and produces slag, and from electric-furnace slag cleaning, which has different feeds, energy inputs, products, and metallurgical objectives [1, 2]. Reported residual-zinc concentrations or recovery values are therefore comparable only when the initial feed, analytical basis, recovery definition, functional unit, and system boundary are consistent. Within this scope, the slag-fuming furnace (SFF) is an established industrial process for removing zinc from molten slag under reducing conditions [3, 4].

In a tuyere-blown SFF, pulverized coal and preheated oxidant are introduced below the slag surface, as illustrated conceptually in Fig. 1. Within the present bath-scale model, coal is carried by a two-way-coupled Lagrangian discrete-element population, and its conversion is represented through finite-rate char oxidation and gasification, which enter the Eulerian phases as heat release and the generation of a CO-rich reducing gas (see section "Governing Equations and Closure Models"). The CO-mediated reaction transfers zinc from the slag to the gas phase. In an industrial furnace, the zinc off-gas is subsequently oxidized, cooled, and treated to collect a zinc-rich fume. These downstream oxidation, condensation, entrainment, and collection processes are outside the computational domain.

The high-momentum gas–coal stream can form a coherent near-tuyere jet or gas cavity before dispersing into a polydisperse plume. The transition between these regimes and the subsequent distribution of coal depend on tuyere momentum, particle size and inertia, gas-to-solids ratio, particle wetting, interfacial deformation, and bath properties.

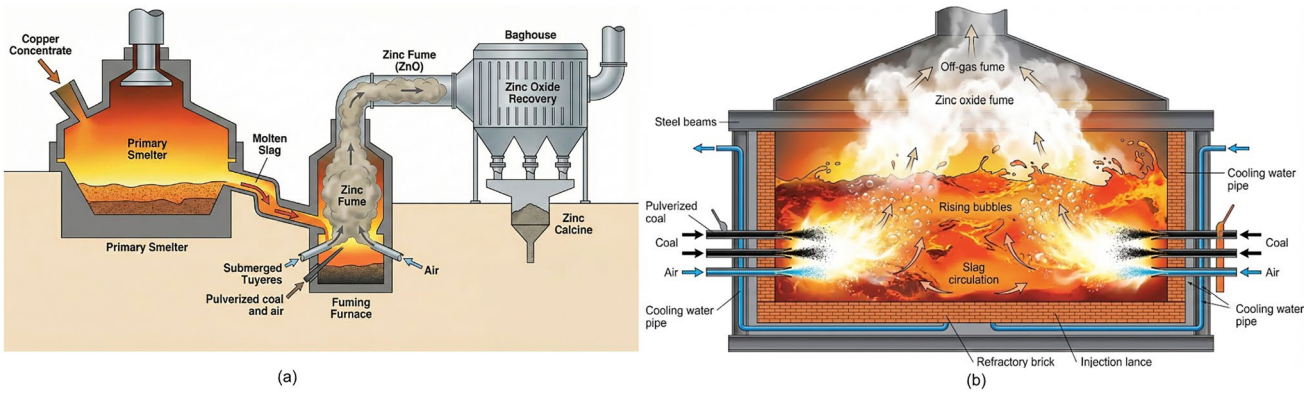

Fig. 1 Conceptual, not-to-scale representation of the slag-fuming process. Panel **a** shows the process route from primary smelting to the downstream recovery of zinc fume. Panel **b** illustrates submerged-tuyere injection, bubble-driven slag circulation, zinc transfer to the gas phase, and off-gas removal. The illustration does not define the computational geometry or the phase structure used in the numerical model

Published industrial models distinguish three coal pathways: transfer of particles from the primary gas into the slag, conversion within the tuyere-gas column or primary bubbles, and rapid transport toward the free surface. For the industrial cycles fitted by Richards and Brimacombe [4], the inferred fractions were approximately 33% entrained in the bath, 55% converted in the tuyere-gas column, and 12% bypassing the main bath-reaction zone. In the high-pressure injection trials analyzed by Cockcroft et al. [5], model-estimated entrainment increased from approximately 25% under the lower-pressure condition to 65–90% under the higher-pressure conditions. Their interpretation depends on the operating conditions and on the criteria used to distinguish entrainment, in-column conversion, and bypass. These fractions are operating-condition-dependent rather than universal model constants. They vary with particle size and density, tuyere momentum, gas-to-solids ratio, bath properties, and the criterion used to distinguish entrainment from bypass. These partitioning studies motivate the present work but are not reproduced by it.

Coal partitioning influences the spatial distributions of carbon conversion, heat release, and reducing-gas generation. It therefore connects tuyere-scale hydrodynamics with the thermal and chemical conditions governing zinc fuming. Near the tuyeres, the rates of carbon partial oxidation, complete oxidation, CO oxidation, and carbon gasification depend on the local oxidant concentration, char reactive area, particle heating and residence time, gas–solid transport, and finite-rate kinetics. Conversely, a strongly CO-rich environment may not generate sufficient heat to compensate for blast heating, endothermic reactions, radiative exchange, and wall cooling. A complete-combustion calculation can therefore provide an upper bound on chemical heat release, whereas the computational fluid dynamics (CFD) model is intended to resolve the local competition between heat generation and reducing-gas availability.

This competition creates a feedback loop across the furnace. Tuyere momentum and coal conversion determine plume structure and the spatial distributions of temperature and CO. These fields affect the rate of ZnO reduction, while reaction heat and heat loss modify the slag temperature. Temperature then influences slag viscosity; an additional compositional response can arise only to the extent prescribed by the implemented property correlation. The resulting rheological state alters jet penetration, bubble rise and residence time, coalescence and breakup, gas hold-up, and the interfacial area available for reaction. The associated changes in mixing and interfacial renewal feed back on carbon conversion and slag-side mass transfer. Accordingly, heat release, chemistry, rheology, and hydrodynamics cannot be treated as independent corrections to an otherwise fixed flow field.

Slag viscosity is a key transport property in the present analysis. For a fully liquid oxide melt, viscosity depends on temperature, bulk composition, oxidation state, and the degree of polymerization of the silicate network. The structural role of an individual oxide is composition-dependent; in particular, Al_2O_3 can exhibit amphoteric behavior, and the influence of iron-containing species depends on their oxidation state and coordination environment. The CFD model does not transport silicate structural units, bridging- and non-bridging-oxygen populations, or redox-resolved iron species. Silicate-network polymerization is therefore used only as a physical interpretation of measured rheological trends, not as a solved variable or as a structural-speciation model [6, 7].

The explicitly modeled composition-changing slag reaction is the CO-mediated reduction of ZnO:

$$ZnO(slag) + CO(g) \rightleftharpoons Zn(g) + CO_2(g). \quad (1)$$

Equation (1) is implemented as a reversible interfacial reaction, so the net rate falls as the local gas approaches the CO/CO_2 ratio in equilibrium with the slag; the back reaction is therefore active wherever the gas becomes locally CO_2-rich. The reaction in Eq. (1) progressively removes ZnO from the liquid oxide mixture. Carbon partial oxidation, CO oxidation, the Boudouard reaction, and the water–gas reaction establish the local CO supply and thermal conditions that support this reduction. The local CO/CO_2 ratio is therefore used as an indicator of the reducing-gas state; the present formulation does not solve oxygen potential as an independent thermodynamic field. Iron-redox chemistry is excluded from the present framework; the reasons and consequences are set out in the section "Treatment of Iron Redox Chemistry."

The modeled slag viscosity is state-dependent: it changes with simulation time because it is evaluated from the instantaneous temperature and the implemented oxide-property mapping, not because an independent time-dependent or thixotropic law is imposed. The closure is empirical and should not be interpreted as a structural-speciation or redox-equilibrium model. The viscosity comparison uses the external industrial zinc–copper-smelting-slag data reported by Mostaghel et al. [7]. Inclusion of the bulk-composition correction improves agreement with that benchmark, but independence from closure selection and adjustment has not been established. It does not demonstrate a particular structural response to ZnO removal. Within the furnace calculations, the compositional contribution to viscosity is limited to that prescribed by the implemented correlation, whereas the temperature-driven rheological response is supported more directly by the benchmark data.

Local measurements in an operating SFF are difficult because of the high temperature, optical opacity, chemically aggressive environment, and restricted physical access. Plant measurements may constrain bath temperature, bulk slag composition, off-gas composition, fume production, tuyere pressure, and cooling duty, but they generally provide less direct information on local velocity, bubble-size distribution, interfacial area, and reaction-rate fields. CFD can relate these quantities through the governing conservation equations and closure models. Interpretation of the resulting fields remains conditional on the interphase-force closures, turbulence treatment, reaction kinetics, transfer correlations, property models, population balance model (PBM) formulation, boundary conditions, numerical verification, and the extent of independent validation.

Earlier furnace-scale CFD studies already coupled several mechanisms relevant to zinc fuming. Huda et al. [3] developed a three-dimensional Eulerian model of a top-submerged-lance furnace that included combustion, chemical reactions, and interphase heat, mass, and momentum transfer. The calculation reproduced the broad temporal trend in slag ZnO and compared the predicted fuming rate with experimental data, although the absolute bath ZnO concentration was overpredicted. Their subsequent tuyere-blown model [8] coupled submerged combustion with bath flow and examined temperature, coal conversion, bypass, and jet penetration.

Complementary studies have examined mechanisms not resolved in the same manner by those furnace-scale models. Sattar et al. [9] coupled multiphase CFD with a sectional PBM to model bubble breakup, coalescence, drainage, and slag-foam behavior. Obiso et al. [10] quantified how temperature-dependent slag properties influence bubble path, deformation, velocity, breakup, and interfacial area in a quiescent bath. Their pilot-scale top-submerged lance (TSL) study [11] subsequently resolved bubble formation, splashing, sloshing, and mixing under deliberately isothermal and nonreactive conditions. Cheng et al. [12] used laboratory fuming experiments and a fitted volumetric liquid-side mass-transfer coefficient to examine ZnO-transfer limitations, while their updated reactive-fraction model [13] coupled a reduced reaction-zone description with ChemApp thermodynamics. Table 1 compares these contributions using the mechanisms explicitly reported by each source and a bounded author comparison of the remaining integration needs.

Previous studies address furnace-scale phenomena separately: Eulerian models couple reaction and heat transfer, interface-resolving simulations capture slag-dependent bubble dynamics, PBMs track bubble populations, and lumped models predict zinc conversion without resolving plume flow. The present study focuses on the coupled reaction kinetics, slag–air-jet interactions, and the transient variation of slag properties under the operating conditions considered. Several additional mechanisms that may influence industrial slag fuming are not resolved in the current framework, including the local oxygen partial pressure, iron-oxide redox chemistry and speciation, and gas-phase transport and reactions within the freeboard above the slag bath. These topics require additional thermodynamic, kinetic, and experimental information and will therefore be investigated in future publications.

Accordingly, this study develops a transient two-dimensional Eulerian–Eulerian representation of an industrial-scale SFF cross-section in which finite-rate carbon and gas-phase reactions, CO-mediated ZnO reduction, reaction heat effects, species transport, gray-gas radiation, state-dependent slag viscosity, and PBM-derived interfacial area density are coupled within one framework. The analysis examines how the evolving thermal field changes slag viscosity and how the concurrent ZnO evolution is associated with tuyere jet penetration, bubble-size distribution,

Table 1 Representative studies of zinc fuming and submerged gas injection, organized by the modeling features relevant to the present work

Study and system	Formulation	Couplings explicitly reported	Evidence or benchmark type	Scope relative to the present model
Huda et al.; TSL zinc fuming [3]	Three-dimensional Eulerian multiphase CFD	Combustion and chemical reactions coupled with interphase heat, mass, and momentum transfer	Slag ZnO trend and fuming rate compared with experimental data; the absolute bath ZnO concentration was overpredicted	–
Huda et al.; tuyere-blown SFF [8]	Three-dimensional Eulerian multiphase CFD with coal conversion	Submerged combustion, chemical reactions, and interphase transport	Jet penetration compared with an isothermal correlation; coal conversion and bypass examined	–
Sattar et al.; bath-smelting slag foam [9]	Multiphase CFD with a sectional population balance and a separate foam phase	Bubble breakup, coalescence, drainage, and foam destruction; no finite-rate ZnO fuming chemistry	Foam height and composition trends compared with available experimental data	Furnace-scale ZnO-reduction chemistry and associated reaction-heat coupling were outside the stated scope
Obiso et al.; bubbles in a quiescent slag bath [10]	Three-dimensional interface-resolving CFD	Nonreactive cases with spatial temperature gradients and temperature-dependent slag properties	Bubble path, shape, velocity, breakup, and interfacial area compared across property descriptions	The study addressed single-bubble behavior in a quiescent, nonreactive bath rather than furnace-scale injection and species conversion
Obiso et al.; pilot-scale TSL bath [11]	Three-dimensional volume of fluid (VOF)	Isothermal, nonreactive flow with constant slag properties	Bubble frequency, splashing, sloshing, and mixing compared with furnace data from the literature	Heat transfer, reaction chemistry, solid feed, and property evolution were deliberately excluded from the pilot-scale flow study
Cheng et al.; bubble-stirred fuming experiments [12]	Laboratory experiments with a lumped kinetic and mass-transfer model	Fitted volumetric liquid-side mass-transfer coefficient, $k_L a$; no furnace-scale CFD	Effects of gas flow, carbon addition, temperature, and slag composition on fuming kinetics	Local plume hydrodynamics and a spatially resolved bubble population were not solved
Cheng et al.; updated reactive-fraction model [13]	Reduced reactive-fraction model coupled with ChemApp thermodynamics	Thermodynamic and kinetic description of an effective reaction zone	Model parameters compared with laboratory experiments; three fuming stages identified	The reduced model did not solve a local momentum field or PBM-derived interfacial-area distribution
Richards and Brimacombe; industrial SFF cycles [4]	Lumped kinetic and mathematical process model	Coal partitioning, bath energy balance, and ZnO reduction kinetics	Fitted to industrial fuming cycles	No local momentum, temperature, or bubble-population field; partitioning fractions are fitted rather than solved
Cockcroft et al.; high-pressure injection trials [5]	Process model with an injection sub-model	Coal entrainment versus bypass as a function of injection pressure	Compared with plant injection trials	Entrainment is inferred from a fitted sub-model; bath hydrodynamics are not resolved
Verscheure et al.; zinc fuming Parts I and II [14, 15]	Multi-zone thermodynamic–kinetic process model	Slag, gas, and coal zones with local equilibrium and iron-redox chemistry	Compared with industrial fuming campaigns	Zone volumes and exchange rates are prescribed; no momentum field or PBM-derived interfacial area
Khartcyzov et al.; furnace energy analysis [16]	Process-scale mass and energy balance	Net reaction, cooling, and off-gas energy terms	Plant energy data	Spatially aggregated; no local hydrodynamics, rheology, or bubble population

gas–slag contact, zinc removal, and the global energy balance. The principal contribution is an integrated numerical architecture for case-specific analysis of these coupled mechanisms.

Model Scope, Computational Configuration, and Assumptions

The objective of the present model is to evaluate the transient thermal budget of a two-dimensional representation of an industrial SFF. Particular attention is given to the coupling between reaction heat, bath temperature, slag properties, multiphase hydrodynamics, and gas–slag heat and mass transfer. The gas and slag are represented as interpenetrating Eulerian phases. Injected coal is represented by a two-way-coupled Lagrangian discrete-element population that exchanges mass, momentum, sensible enthalpy, and reactive carbon with both Eulerian phases; it is not an Eulerian phase and has no phase-fraction transport equation (see section "Governing Equations and Closure Models"). Tuyere injection drives gas holdup and bath recirculation, while a PBM supplies the bubble-size distribution and interfacial-area density required by the transfer closures. Individual bubbles and gas–slag interfaces are therefore not resolved directly. Finite-rate species and reaction-heat source terms are coupled to the energy equation together with radiation and prescribed wall heat extraction. Radiative exchange between the free-surface gas, the freeboard walls, and the slag surface uses a gray-gas participating-media model with a functional absorption coefficient [17]. The furnace dimensions and a graphical representation of the phenomena occurring within the SFF are presented in Fig. 2.

The computational domain is a two-dimensional vertical mid-plane section with a slag depth $Y = 1.5$ m, bath width $W = 2.34$ m, total domain height $H = 8.0$ m, and a tuyere diameter of 0.09 m. The horizontal distance from the tuyere exit to the furnace centerline is therefore $L_h = W/2 = 1.17$ m, which is the length scale used for horizontal jet penetration in the section "Zinc Depletion, Jet Penetration, and the Slag-Viscosity Closure." The Eulerian multiphase calculation is coupled to the S-Gamma PBM used in the solver implementation [18, 19].

The initial slag state is defined using the literature composition in Table 2, normalized to 100 wt%. The simulated physical time is 1800 s. Adaptive time stepping reduces Δt during rapid transients and increases it during slowly varying periods. This strategy improves computational efficiency, but temporal accuracy also depends on the time-integration scheme, the permitted time-step range, the controller criterion, and a time-step-sensitivity assessment. These numerical settings are therefore distinct from the physical duration of the calculation.

Density and surface tension are evaluated as functions of temperature and the transported oxide composition, whereas the documented heat-capacity and thermal-conductivity closures depend only on temperature.

Initial and boundary conditions are summarized in Table 3.

Species transport is solved for the represented gas-phase and slag components. Activated reactions generate local species source terms, while the corresponding heat effects enter the energy equation from the same local reaction rates. The finite-rate expressions are supplied in Chemkin format, and temperature-dependent species thermochemistry is evaluated using the Ansys Chemkin database [21]. The reaction mechanism and thermodynamic data file used in the calculation are provided in the reaction file. An in-house Python interface was developed to bridge Ansys Chemkin and STAR-CCM+, enabling the Chemkin species definitions, reaction mechanism, and thermodynamic data to be parsed, reformatted, and transferred into a STAR-CCM+-compatible structure while preserving species names, stoichiometric coefficients, reaction-rate parameters, and thermochemical properties. Standard reaction enthalpies are evaluated from the species data using Hess's law:

$$\Delta_r H^\circ(T) = \sum_{i \in \text{products}} \nu_i \Delta_f H_i^\circ(T) - \sum_{i \in \text{reactants}} \nu_i \Delta_f H_i^\circ(T), \quad (2)$$

where ν_i is the positive stoichiometric magnitude of species i in the corresponding product or reactant sum, and $\Delta_f H_i^\circ(T)$ is its standard enthalpy of formation at temperature T. The resulting chemical-energy source is evaluated from the local reaction rate. The transported energy variable is a sensible enthalpy and carries no formation enthalpies, so the chemical source of Eq. (13) is applied exactly once. The phase allocation and sign convention adopted for each source are stated in the section "Governing Equations and Closure Models," and the achieved global species and energy balance closures are reported in the section "Verification and Validation Status."

Table 4 lists the reactions activated in the baseline calculation. Reactions excluded from the baseline, including direct carbon reduction of ZnO, zinc-fume oxidation, and sulphate decomposition or formation, are listed in Table 4 with an explicit excluded status so that the active set is unambiguous. The reported reaction enthalpies are calculated at 1500 K from the exact thermodynamic file used by the solver, with the single exception noted in footnote a.

The only transported change in slag composition in the baseline calculation is the CO-mediated removal of ZnO.

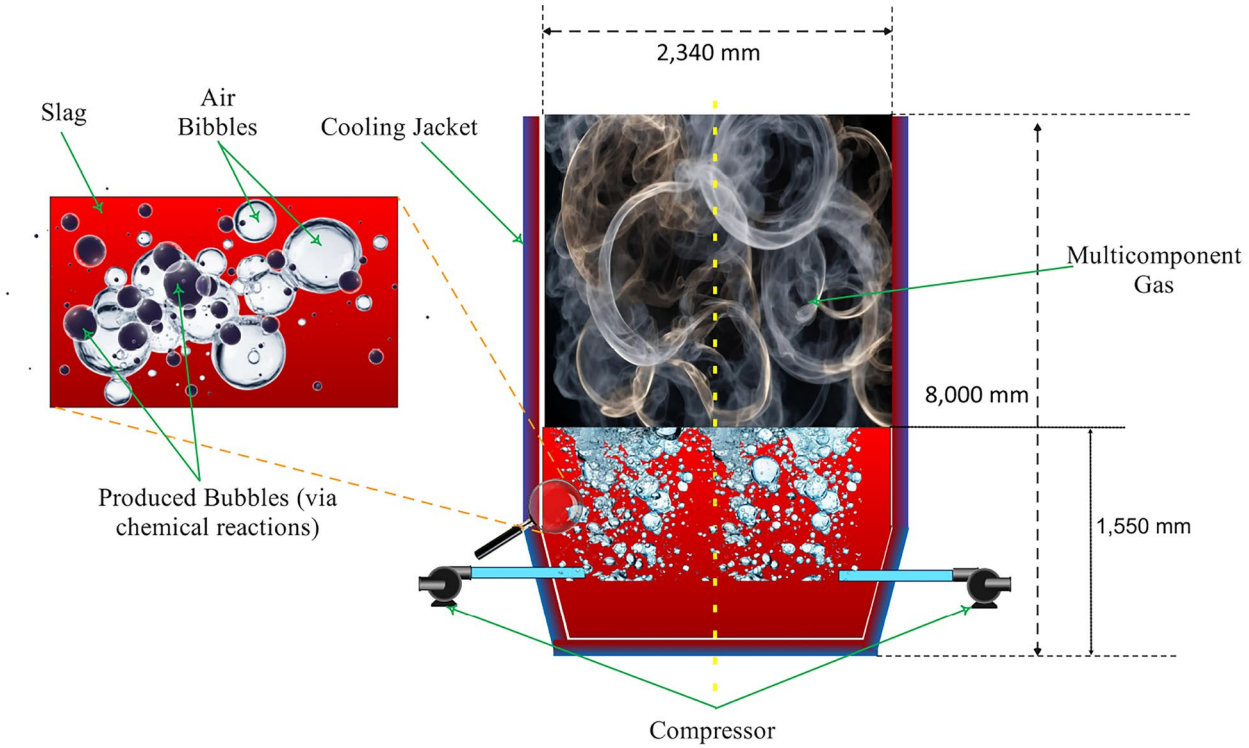

(a)

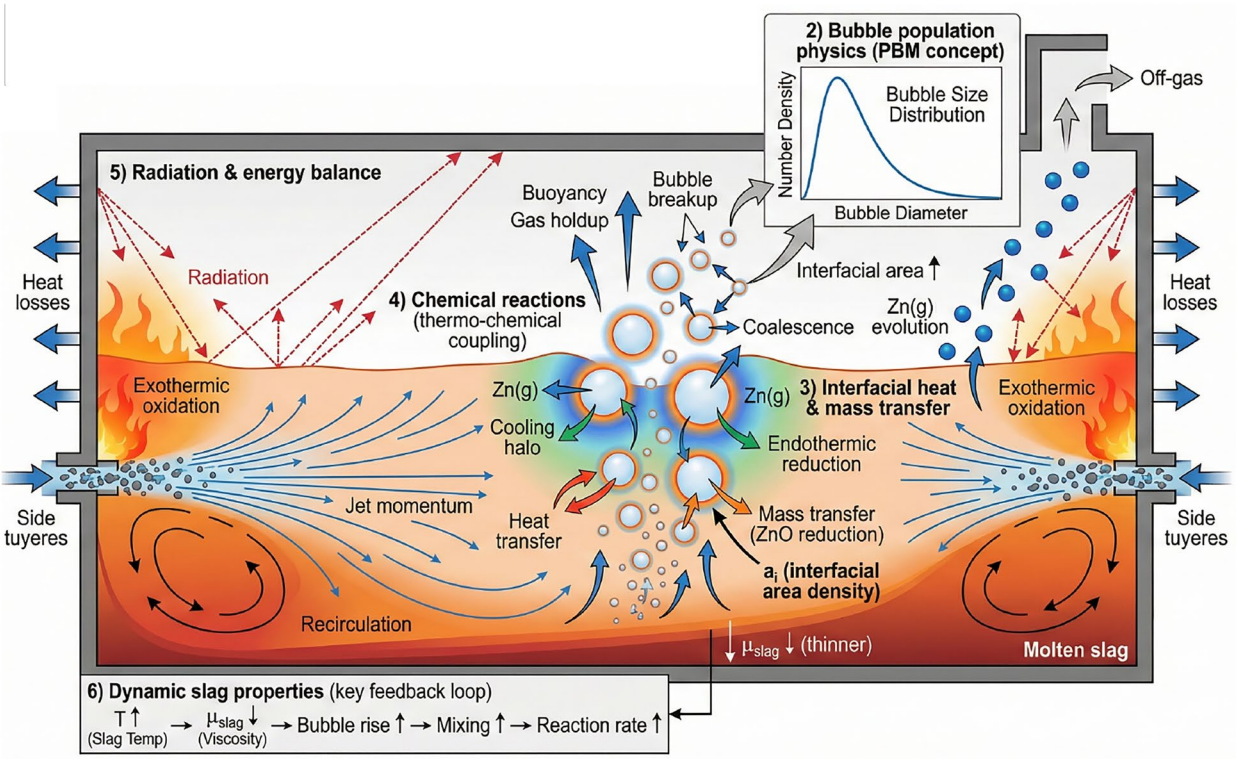

(b)

Fig. 2 Representation of the slag-fuming model: **a** furnace-domain configuration and **b** conceptual coupling of the thermo-reactive Eulerian–Eulerian framework

Table 2 Representative literature-based initial oxide composition used as the numerical proxy, normalized to 100 wt%

Oxide	FeO_x equiv	SiO_2	CaO	Al_2O_3	ZnO	MgO	CuO	MnO	P_2O_5	Na_2O	TiO_2	K_2O	Cr_2O_3
Content (wt%)	38.51	21.17	16.25	7.75	6.27	2.61	2.09	1.34	1.11	1.02	0.72	0.58	0.58

Data reproduced from Wang and Erdenebold [20]; the composition is that of a carbon-reduced copper slag reported for a recycling study and is used here only as a numerical proxy for an industrial fuming feed. It is not the Boliden slag from which the plant ZnO data in Fig. 5c were taken, and the two are compared on a normalized basis only. Original data are available based on reasonable request

Table 3 Boundary conditions, initial conditions, and reproducibility-critical inputs for the baseline simulation

Input	Value or implementation	Unit or basis	Scope and disclosure note
Air-inlet and coal-injection temperature	500	K	–
Initial slag temperature	1500	K	The initial bath field is spatially uniform
Initial slag depth	1.5	m	Used to convert dimensionless jet penetration y/Y to meters
Initial slag viscosity	0.4	Pa s	Initialization value before the first local property update
Initial slag density	3500	kg/m^3	Initialization value before the first local property update
Initial slag thermal conductivity	2.5	W/(m K)	Initialization value; subsequent updates follow the temperature-only conductivity closure specified below
Initial physical coal-particle diameter	10	μm	–
Coal phase and conversion inputs	–	Model definition	The phase representation, proximate and ultimate analyses, char density, reactive-area basis, devolatilization treatment, ash transfer, and kinetic parameters are required to reconstruct coal conversion

Carbon oxidation, CO oxidation, and the Boudouard reaction determine the local heat release and CO inventory. The water–gas shift and carbon–steam gasification reactions are active only when H_2O is explicitly present in the inlet or generated by another represented mechanism; in the baseline inlet composition they are therefore inactive, and they contribute no term to the energy audit in Table 6. The CO/CO_2 ratio is treated as a gas-composition indicator and is not converted into a thermodynamic oxygen potential.

Table 5 records the thermophysical closures used for the slag phase and distinguishes their mathematical dependencies from their physical validity.

At each time step, the coupled equations are advanced through an outer nonlinear, Picard-type iteration. Within an outer iteration, the solver updates slag properties, evaluates reaction rates and paired mass and energy source terms, solves species and energy transport, advances Eulerian momentum and continuity, and refreshes the unsteady Reynolds-averaged Navier–Stokes (URANS) turbulence fields. The PBM moments and interfacial area are updated consistently with the multiphase state before the next outer iteration. Time integration employed an adaptive time-step strategy over the 1800 s simulation. The calculation is initialized with a small time step of $\Delta t = 1 \times 10^{-7}\ s$ to resolve the rapid jet and plume development. The time step is subsequently increased during slowly varying periods and reduced when rapid transients or convergence difficulties are detected. Figure 3 presents a simplified graphical representation of the simulation algorithm and the associated data flow adopted in this study. For clarity, some secondary model features and implementation details are omitted.

The calculation is used to examine interactions among the represented mechanisms under one prescribed two-dimensional configuration. Its validation status is stated once, in the section "Verification and Validation Status." The consequences of the two-dimensional reduction and of the uniform wall heat flux are set out in the section "Modeling Limitations."

Governing Equations and Closure Models

In the present study, gas and molten slag are represented as the two momentum-carrying Eulerian fluid phases, with $q \in \{g, \ell\}$. Injected coal is represented separately by a two-way-coupled Lagrangian discrete-element method (DEM) population. Coal is therefore not included in the Eulerian phase index q and does not have an Eulerian phase-fraction transport equation. Under the dilute point-particle approximation adopted here, coal-particle volume displacement is neglected and the Eulerian fluid fractions satisfy $\alpha_g + \alpha_\ell = 1$. The DEM particles nevertheless carry mass, momentum, sensible enthalpy, and reactive carbon, and exchange these quantities with the Eulerian gas and slag phases through cell-based

Table 4 Reactions activated in the baseline finite-rate mechanism and their standard reaction enthalpies at 1500 K (active/excluded reactions)

Reaction	$\Delta_r H°$ (kJ/mol reaction)	Character	Status in the present framework
Fe_2O_3(slag) + CO(g) ⇌ 2 FeO(slag) + CO_2 (g)[a]	≈ +35	Endothermic	Excluded from the baseline; iron redox is not solved
ZnO(slag) + C(s) → Zn(g) + CO(g)	≈ +350	Endothermic	Excluded from the baseline; direct carbon–slag reduction is not represented
ZnO(slag) + CO(g) ⇌ Zn(g) + CO_2(g)	$\Delta_r H°$	Endothermic in the forward direction	Active reversible interfacial reaction; the net rate is evaluated and vanishes when $Q_r = K_r(T)$[b]
CO(g) + 1/2 O_2(g) → CO_2(g)	≈ −280	Exothermic	Active gas-phase oxidation reaction
C(s) + 1/2 O_2(g) → CO(g)	≈ −115	Exothermic	Active carbon partial-oxidation reaction
C(s) + O_2(g) → CO_2(g)	≈ −396	Exothermic	Active carbon oxidation reaction
C(s) + CO_2(g) ⇌ 2 CO(g)	≈ +165	Endothermic	Active Boudouard reaction
CO(g) + H_2O(g) ⇌ CO_2(g) + H_2(g)	≈ −30	Mildly exothermic	Conditional baseline reaction; it is inactive when no water enters the represented system
C(s) + H_2O(g) → CO(g) + H_2(g)	≈ +135	Endothermic	Conditional baseline reaction; it is inactive when no water enters the represented system
2 Zn(g) + O_2(g) → 2 ZnO(s)	$\Delta_r H°$	Exothermic	Excluded from the baseline; zinc-fume reoxidation occurs downstream of the computational domain
$ZnSO_4$(s) → ZnO(s) + SO_2(g) + 1/2 O_2(g)	≈ +286	Endothermic	Optional mechanism; inactive in the baseline bath calculation
ZnO(s) + SO_2(g) + 1/2 O_2(g) → $ZnSO_4$(s)	≈ −286	Exothermic	Optional reverse mechanism; inactive in the baseline bath calculation

Positive $\Delta_r H°$ denotes an endothermic reaction, i.e., heat absorbed; note that Table 6 uses the opposite convention, in which positive values denote heat released to the slag bath

[a]Recalculated from standard condensed-phase formation enthalpies, $Fe_2O_3 + CO \rightarrow 2\ FeO + CO_2$ is close to thermoneutral at 298 K (about −3 kJ/mol reaction)

[b]As reduction proceeds, the reaction quotient Q_r approaches the temperature-dependent equilibrium constant $K_r(T)$, reducing the net ZnO conversion rate. The net rate vanishes when $Q_r = K_r(T)$. Equilibrium therefore defines a thermodynamic upper bound under the specified temperature, pressure, and slag composition. However, the degree to which this bound is approached during the finite fuming cycle depends on the gas–slag interfacial area, mass-transfer resistance, reaction kinetics, and gas residence time. The equilibrium conversion is independent of interfacial area, whereas the conversion attained within 1800 s is not. Because the reaction is reversible, the back reaction Zn(g) + CO_2(g) → ZnO(slag) + CO(g) is active wherever the local gas becomes CO_2-rich, and it reduces the net removal rate in the upper bath

Table 5 Thermophysical property closures specified for the slag phase

Parameter	Correlation, implementation, and validity
$\mu(T, \mathbf{w})$	The model-specific expression supplied for the calculation is $\mu_{\text{model}}\ [\text{P}] = 0.00601 \exp\left[\left(\frac{1283.45}{T} - 3.2788\right)K_{v,\text{model}} + \frac{11422.61}{T}\right]$, $\mu\ [\text{Pa s}] = 0.1\ \mu_{\text{model}}$, with T in kelvin [22]
$\rho(T, \mathbf{w})$	$\rho_{\text{slag}}(T, \mathbf{w}) = \left[\sum_{i\in\mathcal{I}} \frac{\widetilde{w}_i}{\rho_i^{\ell}(T)}\right]^{-1}$, $\widetilde{w}_i = \frac{w_i}{\sum_{j\in\mathcal{I}} w_j}$, where $\mathcal{I}$ = { FeO, Fe_2O_3 (equiv.), SiO_2, CaO, MgO, Al_2O_3, ZnO}. Here $\rho_i^{\ell}(T)$ is the liquid-component density in kg/m^3
$k(T)$ or $\lambda(T)$	$\lambda(T) = A_\lambda \exp\left(-\frac{B_\lambda}{T}\right)$
$c_p(T)$	$c_p(T) = 0.60 + 2.8 \times 10^{-4} T$ in kJ/(kg K), with T in kelvin
$\sigma(T, \mathbf{x})$	$\ln\left(\frac{\sigma_{\text{slag}}(T, \mathbf{x})}{\sigma_{\text{ref}}}\right) = \sum_i x_i \ln\left(\frac{\sigma_i(T)}{\sigma_{\text{ref}}}\right)$, $\sigma_{\text{slag}} = \prod_i \sigma_i(T)^{x_i}$, where $x_i = \frac{w_i/M_i}{\sum_j w_j/M_j}$, $\sum_i x_i = 1$. The reference value σ_{ref} makes the logarithms dimensionless and cancels from the equivalent geometric-mean expression

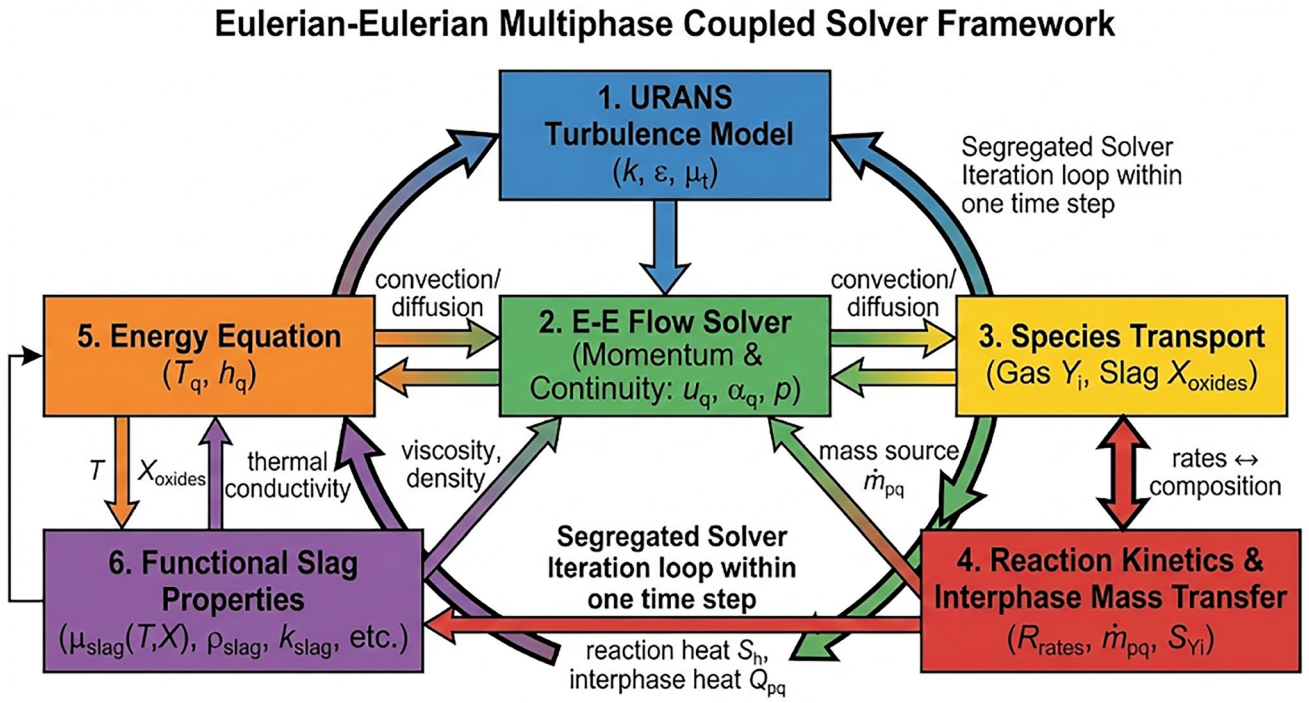

Fig. 3 Coupled solution sequence for the Eulerian–Eulerian thermo-reactive multiphase framework. This figure is just a conceptual design of dataflow in this study

source terms. The equations in this section are written for gas and molten slag as the two momentum-carrying Eulerian phases, with phase index $q \in \{g, \ell\}$ and $\alpha_g + \alpha_\ell = 1$. The Eulerian–Eulerian formulation solves phase-averaged mass, momentum, and sensible-enthalpy equations for the gas and slag phases [19, 23]. Interphase exchange terms are defined per unit mixture volume. A positive $\dot{m}_{p\to q}$ denotes mass transferred from phase p to phase q.

$$\frac{\partial}{\partial t}\left(\alpha_q \rho_q\right) + \nabla \cdot \left(\alpha_q \rho_q \mathbf{v}_q\right) = \sum_{p \neq q} \left(\dot{m}_{p\to q} - \dot{m}_{q\to p}\right) + S^{\text{ext}}_{\rho,q}, \quad (3)$$

where ρ_q and $\mathbf{v}_q$ are the density and velocity of phase q, respectively. Internal gas–slag transfer cancels when Eq. (3) is summed over both phases. The term $S^{\text{ext}}_{\rho,q}$ is reserved for exchange with a representation that is not included in $q \in \{g, \ell\}$, such as a prescribed solid-carbon source. Any nonzero external source must be included in the reported global mass and elemental balances.

The corresponding phase-momentum equation is

$$\begin{aligned}\frac{\partial}{\partial t}\left(\alpha_q \rho_q \mathbf{v}_q\right) &+ \nabla \cdot \left(\alpha_q \rho_q \mathbf{v}_q \otimes \mathbf{v}_q\right) \\ &= -\alpha_q \nabla p + \nabla \cdot \boldsymbol{\tau}_q + \alpha_q \rho_q \mathbf{g} + \sum_{p \neq q} \mathbf{M}_{p\to q} \\ &\quad + \sum_{p \neq q} \left(\dot{m}_{p\to q}\mathbf{v}_{p\to q} - \dot{m}_{q\to p}\mathbf{v}_{q\to p}\right) + S^{\text{ext}}_{\rho,q}\mathbf{v}_{S,q},\end{aligned} \quad (4)$$

where p is the pressure shared by the phases, $\mathbf{g}$ is gravitational acceleration, and $\mathbf{M}_{p\to q}$ is the interphase force on phase q due to phase p. Pairwise interphase forces satisfy $\mathbf{M}_{p\to q} = -\mathbf{M}_{q\to p}$. The velocity $\mathbf{v}_{p\to q}$ is the velocity assigned to transferred mass; the baseline uses the donor-phase velocity, $\mathbf{v}_{p\to q} = \mathbf{v}_p$. The final term preserves momentum when an external volumetric mass source is used. It is zero when injection is imposed only through boundary conditions.

The deviatoric effective stress is written as

$$\boldsymbol{\tau}_q = \alpha_q \mu_{q,\text{eff}}\left[\nabla \mathbf{v}_q + \left(\nabla \mathbf{v}_q\right)^{\top} - \frac{2}{3}\left(\nabla \cdot \mathbf{v}_q\right)\mathbf{I}\right], \quad (5)$$

where $\mu_{q,\text{eff}}$ is the effective viscosity of phase q, $\mathbf{I}$ is the identity tensor, and $\top$ denotes the transpose. The liquid and gas effective viscosities are

$$\mu_{\ell,\text{eff}} = \mu_\ell + \mu^{\text{eff}}_{t,\ell}, \qquad \mu_{g,\text{eff}} = \mu_g + \mu_{t,g},$$

where $\mu^{\text{eff}}_{t,\ell}$ is defined in Eq. (17) and already contains the bubble-induced contribution μ_{BIT}, which is therefore not added a second time here. The molecular slag viscosity μ_ℓ is evaluated locally using the verified closure in Table 5. The value 0.4 Pa s in Table 3 is used only for initialization and is replaced at the first property update. For the interphase-force definitions, the molten slag is the continuous phase c, the gas is the dispersed phase d, and $\mathbf{u}_r = \mathbf{v}_d - \mathbf{v}_c$. The

force on the dispersed phase due to the continuous phase is decomposed as

$$\mathbf{M}_{c\to d} = \mathbf{F}_D + \mathbf{F}_L + \mathbf{F}_{\mathrm{vm}} + \mathbf{F}_{\mathrm{wl}} + \mathbf{F}_{\mathrm{td}}, \qquad \mathbf{M}_{d\to c} = -\mathbf{M}_{c\to d}. \tag{6}$$

The drag force is represented in the general form

$$\mathbf{F}_D = -K_D \mathbf{u}_r, \qquad K_D = \frac{3}{4}\,\frac{\alpha_c \alpha_d \rho_c C_D f_h}{d_b}\,|\mathbf{u}_r|, \tag{7}$$

where C_D is the selected drag coefficient and f_h is any activated swarm or hindrance correction. The lift force is

$$\mathbf{F}_L = -C_L \rho_c \alpha_d\, \mathbf{u}_r \times \left(\nabla \times \mathbf{v}_c\right), \tag{8}$$

with the sign convention fixed by $\mathbf{u}_r = \mathbf{v}_d - \mathbf{v}_c$. The virtual-mass force is

$$\mathbf{F}_{\mathrm{vm}} = C_{\mathrm{vm}} \rho_c \alpha_d \left(\frac{D_c \mathbf{v}_c}{Dt} - \frac{D_d \mathbf{v}_d}{Dt} \right), \tag{9}$$

where $D_q/Dt = \partial/\partial t + \mathbf{v}_q \cdot \nabla$. The wall-lubrication and turbulent-dispersion forces are written generically as

$$\begin{aligned} \mathbf{F}_{\mathrm{wl}} &= C_{\mathrm{wl}} \rho_c \alpha_d |\mathbf{u}_{r,\parallel}|^2 \mathbf{n}_w, \\ \mathbf{F}_{\mathrm{td}} &= -C_{\mathrm{td}} \rho_c k_c \nabla \alpha_d, \end{aligned} \tag{10}$$

where $\mathbf{n}_w$ points away from the wall and $\mathbf{u}_{r,\parallel}$ is the wall-tangential slip velocity. As written, $\mathbf{F}_{\mathrm{wl}}$ omits the $1/d_b$ factor of the standard Antal form, so C_{wl} carries units of 1/m rather than being dimensionless. Equations (7)–(10) define the force basis and sign convention. The sensible-enthalpy equation for phase q is written in the low-Mach form

$$\begin{aligned} &\frac{\partial}{\partial t}\left(\alpha_q \rho_q h_{s,q}\right) + \nabla \cdot \left(\alpha_q \rho_q \mathbf{v}_q h_{s,q}\right) \\ &\quad = -\nabla \cdot \left(\alpha_q \mathbf{q}_q\right) + \sum_{p\neq q} Q_{p\to q} \\ &\qquad + \sum_{p\neq q} \left(\dot{m}_{p\to q} h_{s,p\to q} - \dot{m}_{q\to p} h_{s,q\to p}\right) \\ &\qquad + S_{h,q}^{\mathrm{chem}} + S_{h,q}^{\mathrm{rad}} + S_{h,q}^{\mathrm{ext}}, \end{aligned} \tag{11}$$

where $h_{s,q}$ is sensible specific enthalpy. The interphase heat source is $Q_{p\to q} = a_i h_{pq}(T_p - T_q)$ and satisfies $Q_{p\to q} = -Q_{q\to p}$ when the same interfacial area and heat-transfer coefficient are used for both phases. For spherical bubbles,

$$a_i = \frac{6\alpha_g}{d_{32}},$$

which is an area-equivalent approximation when the bubbles are deformed or the gas holdup is high. Pressure work, viscous dissipation, and kinetic-energy transport are neglected in Eq. (11); this approximation must be consistent with the low-Mach and sensible-enthalpy options activated in the solver. Jacket cooling is imposed through the wall boundary condition and is not duplicated as a volumetric source. The radiative source is retained only in the phase or region in which the selected radiation model deposits energy.

The conductive and turbulent heat flux is

$$\mathbf{q}_q = -\lambda_{q,\mathrm{eff}} \nabla T_q, \qquad \lambda_{q,\mathrm{eff}} = \lambda_q + \frac{c_{p,q}\mu_{t,q}^{(h)}}{\mathrm{Pr}_{t,q}}, \tag{12}$$

where λ_q is the molecular thermal conductivity and $\mu_{t,q}^{(h)}$ is the turbulent viscosity used specifically for heat transport. Reaction heat is assembled once from the common rate of progress used by the species equations:

$$S_{h,q}^{\mathrm{chem}} = -\sum_r \chi_{r,q}\, \Delta_{\mathrm{r}} H_r^{\circ}(T)\, \dot{\omega}_r, \qquad \sum_q \chi_{r,q} = 1, \tag{13}$$

where $\dot{\omega}_r$ is the rate of progress per unit mixture volume and $\chi_{r,q}$ allocates the heat of reaction to the participating phases without double counting. With $\dot{\omega}_r$ in kmol/(m^3 s) and $\Delta_{\mathrm{r}} H_r^{\circ}$ in J/kmol, Eq. (13) gives W/m^3. An exothermic reaction has $\Delta_{\mathrm{r}} H_r^{\circ} < 0$ and therefore produces a positive source. Equation (13) is appropriate only when formation enthalpies are not already embedded in the transported energy variable.

Turbulence Treatment

The continuous slag phase is modeled with the realizable k–ϵ URANS closure of Shih et al. [24], as implemented in STAR-CCM+ [19]. The original model improved several single-phase benchmark predictions, including planar and round free-shear flows, relative to the standard k–ϵ model; this does not constitute validation for the present gas–slag furnace.

The phase-averaged transport equations are

$$\begin{aligned} \frac{\partial}{\partial t}\left(\alpha_\ell \rho_\ell k\right) + \nabla \cdot \left(\alpha_\ell \rho_\ell \mathbf{v}_\ell k\right) &= \nabla \cdot \left[\alpha_\ell \left(\mu_\ell + \frac{\mu_{t,\ell}}{\sigma_k}\right)\nabla k\right] \\ &\quad + \alpha_\ell \left(G_k - \rho_\ell \varepsilon\right) + S_{k,\mathrm{BIT}}, \end{aligned} \tag{14}$$

$$\begin{aligned} &\frac{\partial}{\partial t}\left(\alpha_\ell \rho_\ell \varepsilon\right) + \nabla \cdot \left(\alpha_\ell \rho_\ell \mathbf{v}_\ell \varepsilon\right) \\ &\quad = \nabla \cdot \left[\alpha_\ell \left(\mu_\ell + \frac{\mu_{t,\ell}}{\sigma_\varepsilon}\right)\nabla \varepsilon\right] \\ &\qquad + \alpha_\ell \rho_\ell \left[C_1 S_\ell \varepsilon - C_2 \frac{\varepsilon^2}{k + \sqrt{\nu_\ell \varepsilon}}\right] + S_{\varepsilon,\mathrm{BIT}}, \end{aligned} \tag{15}$$

where

$$S_{ij} = \frac{1}{2}\left(\frac{\partial v_{\ell,i}}{\partial x_j} + \frac{\partial v_{\ell,j}}{\partial x_i}\right), \qquad S_\ell = \sqrt{2 S_{ij} S_{ij}},$$

$$G_k = \mu_{t,\ell} S_\ell^2, \qquad \nu_\ell = \frac{\mu_\ell}{\rho_\ell}.$$

The model constants are $C_1 = \max[0.43, \eta/(\eta+5)]$, $\eta = S_\ell k/\varepsilon$, $C_2 = 1.9$, $\sigma_k = 1.0$, and $\sigma_\varepsilon = 1.2$. The shear-induced eddy viscosity is

$$\mu_{t,\ell} = \rho_\ell C_\mu \frac{k^2}{\varepsilon}, \tag{16}$$

where C_μ is evaluated from the local strain and rotation invariants in the realizable formulation rather than prescribed as 0.09. The exact STAR-CCM+ implementation and any rotation correction are fixed by the reported software version.

Bubble-induced turbulence can be represented by an algebraic Sato viscosity, by explicit production and dissipation sources in Eqs. (14) and (15), or by another documented multiphase-turbulence model. These treatments are not interchangeable. In the present calculation, bubble-induced turbulence is represented exclusively by the algebraic Sato-type closure [25] given below, which augments the liquid-phase turbulent viscosity with a bubble-induced contribution:

$$\mu_{t,\ell}^{\text{eff}} = \mu_{t,\ell} + \mu_{\text{BIT}}, \qquad \mu_{\text{BIT}} = C_{\mu,\text{BIT}} \rho_\ell \alpha_g d_{32} \left| \mathbf{v}_g - \mathbf{v}_\ell \right|, \qquad C_{\mu,\text{BIT}} = 0.6. \tag{17}$$

The substitution $d_b = d_{32}$ applies a monodisperse algebraic closure to a polydisperse population and is an empirical area-equivalent approximation. Under the Sato-only option, the explicit wake-production sources are

$$S_{k,\text{BIT}} = 0, \qquad S_{\epsilon,\text{BIT}} = 0. \tag{18}$$

The dispersed gas phase uses an algebraic turbulence-response model rather than a second transported k–ϵ system:

$$\mu_{t,g} = C_{t,g} \frac{\rho_g}{\rho_\ell} \mu_{t,\ell}. \tag{19}$$

Setting $C_{t,g} = 1$ imposes equal turbulent kinematic viscosities in the two phases, and this value was used in all reported calculations.

Coal-Particle Modeling

Injected coal is represented by a two-way-coupled Lagrangian discrete-element method (DEM), whereas the gas and molten slag are treated as Eulerian phases. Coal is therefore not included in the Eulerian phase index and has no Eulerian phase-fraction transport equation. Under the dilute point-particle approximation, particle-volume displacement is neglected, and $\alpha_g + \alpha_\ell = 1$. Each computational particle carries its position, velocity, mass, temperature, and reactive-carbon inventory.

The translational motion of particle p is governed by

$$\frac{\mathrm{d}\boldsymbol{x}_p}{\mathrm{d}t} = \boldsymbol{u}_p, \qquad m_p \frac{\mathrm{d}\boldsymbol{u}_p}{\mathrm{d}t} = m_p \boldsymbol{g} + \boldsymbol{F}_{f\to p} + \sum_j \boldsymbol{F}_{pj}^{c} + \sum_w \boldsymbol{F}_{pw}^{w}, \tag{20}$$

where $\boldsymbol{F}_{f\to p}$ denotes the fluid–particle interaction force, while $\boldsymbol{F}_{pj}^{c}$ and $\boldsymbol{F}_{pw}^{w}$ represent particle–particle and particle–wall contact forces, respectively. Particle heating and carbon conversion are evaluated from the local fluid conditions and the activated finite-rate reactions. The resulting mass, momentum, species, and enthalpy exchanges are mapped to the surrounding Eulerian control volumes as equal-and-opposite source terms, thereby providing two-way coupling between the coal population and the gas–slag flow [26].

Additional theoretical background is provided in Appendix.

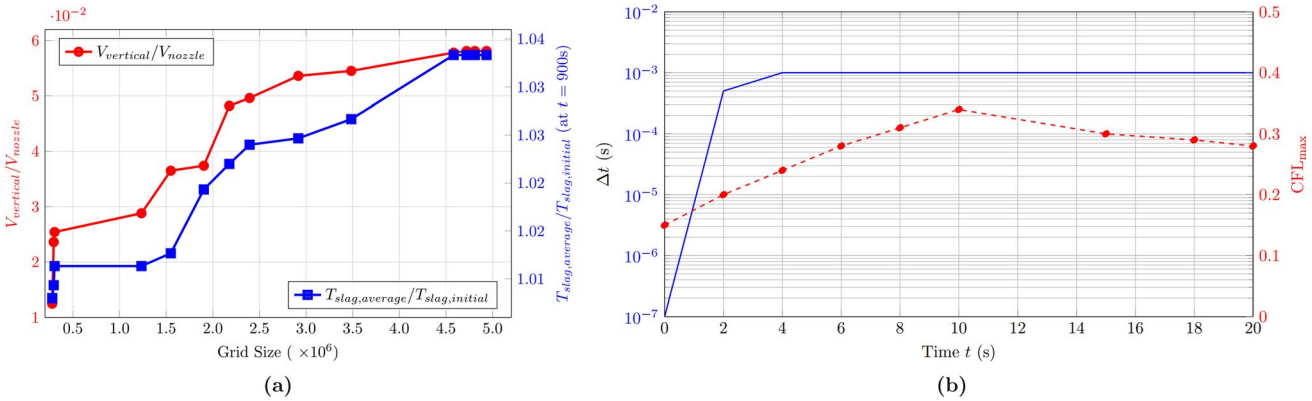

Fig. 4 Mesh- and time-step-sensitivity analyses: **a** convergence of normalized vertical velocity and average slag temperature with increasing mesh resolution (evaluated at $t = 900$ s); **b** adaptive time-step history and maximum Courant–Friedrichs–Lewy (CFL) number during the initial transient

Verification and Validation Status

Figure 4a illustrates the effect of spatial resolution on two macroscopic variables: the dimensionless vertical velocity ($V_{vertical}/V_{nozzle}$) and the normalized average slag temperature ($T_{slag,average}/T_{slag,initial}$) evaluated at $t = 900$ s. The mesh resolution was varied from approximately 0.28×10^6 to nearly 5.0×10^6 cells. Coarse grids below 2.5×10^6 cells show clear sensitivity, consistent with under-resolved plume gradients and numerical diffusion. Above approximately 3.0×10^6 cells, both monitored quantities approach an asymptotic trend, and the selected grid of 4.6×10^6 cells gives changes below 1% relative to the next refinement for these two metrics. The temperature plotted in panel (a) is a slag-volume-weighted average. The mass-weighted average used in the section "Reaction-Driven Temperature Evolution and Partial Energy Audit" is the appropriate basis for an energy analysis, and the two differ at the same instant: panel (a) gives $T/T_0 \approx 1.03$ at $t = 900$ s, whereas Fig. 9a gives 1.00 at $t/t_{end} = 0.50$.

Two qualifications apply to that statement. First, the finest pair of grids, 4.6×10^6 and 5.0×10^6 cells, differ by a linear refinement ratio of only $r \approx 1.04$ in two dimensions, which is well below the $r \geq 1.3$ normally required for a convergence claim. Second, 4.6×10^6 cells over the present two-dimensional domain correspond to a mean cell edge of approximately 2 mm, which is comparable to the Sauter mean diameter predicted by the population balance in the section "Bubble-Scale Estimates and PBM Distribution."

Figure 4b shows the Courant–Friedrichs–Lewy (CFL) study. The simulation is initialized with $\Delta t = 10^{-7}$ s, and the time step increases as the early jet/plume transient develops. The plotted interval covers only $t = 0$–20 s, whereas the total simulated physical time is 1800 s. Physical validation remains partial. Figure 5a and b compare dimensionless velocity and coal-mass profiles against the numerical benchmark of Huda et al. [8]. These are code-to-code benchmarks: the reference profiles are themselves CFD predictions, computed on a different geometry with different closures. Deviations reach 19% in velocity and 25% in coal mass, so the comparison establishes agreement in profile shape only.

Figure 5c reports two experimental ZnO concentration histories. The measured samples were taken from the Boliden furnace, whose slag differs in composition from the literature proxy in Table 2; the comparison is therefore restricted to the normalized depletion trend and does not test absolute ZnO levels. Figure 5d compares the CFD-predicted cooling-system temperature gradient with an experimental baseline and gives a normalized value of 1.217, corresponding to a 21.7% overprediction. This is a useful plant-scale thermal check, but a single scalar heat-removal comparison cannot validate the full thermo-reactive multiphase model.

Simulation Results and Discussion

This section reports the thermal, hydrodynamic, chemical, and bubble-population-related results and post-processing over the 1800 s fuming cycle. Dimensionless times are defined as t/t_{end}, with $t_{end} = 1800$ s.

Zinc Depletion, Jet Penetration, and the Slag-Viscosity Closure

Figure 6 compares instantaneous streamlines and the normalized local CO_2 source at $t = 15$ s and $t = 100$ s. At 15 s, the displayed streamlines are concentrated mainly in the upper and central bath, whereas fewer streamlines pass through the lower region. At 100 s, the displayed recirculation pattern extends farther into the lower bath. These are qualitative observations from two snapshots; a quantitative statement that circulation becomes stronger would require, for example, a common velocity scale, circulation flux, turbulent kinetic energy, mixing time, or zone-volume measure.

Based on the post-processed temperature distribution and the instantaneous flow and reaction-source fields shown in Fig. 6, the furnace domain is interpreted in terms of three qualitative hydrodynamic regions: a near-tuyere, plume-dominated region (Z1); a bulk recirculation region governed by the principal circulation structure (Z2); and a lower region characterized by comparatively sparse streamlines (Z3). These regions are introduced solely as descriptive aids for discussing the spatial organization of the instantaneous solution and should not be interpreted as formally defined reactor compartments.

Submerged injection generates strong local momentum transfer, phase interaction, turbulent transport, and recirculation, while the chemical-reaction and heat-transfer source terms introduce spatially varying thermal sources and sinks. Their coupled action produces a nonuniform transient temperature field within the bath. The property-update loop through which this field feeds back on the flow is described in the section "Model Scope, Computational Configuration, and Assumptions" and Appendix section "Property-Update Coupling" and is not repeated here.

Figure 7a shows a monotonic decrease in the reported slag-phase ZnO concentration over the 1800 s operating cycle. The concentration declines from approximately 6.27 wt% at $t/t_{end} = 0$ to 4.22 wt% at $t/t_{end} = 1$, representing an absolute reduction of 2.05 percentage points and a relative decrease of approximately 32.7%. The intermediate concentrations are approximately 6.02, 5.72, 5.36, 5.24, 4.96, and 4.55 wt% at about 257, 514, 771, 1029, 1286, and 1543 s, respectively. The cycle-averaged concentration-change rate is therefore approximately -1.14×10^{-3} wt% s^{-1}, equivalent to -6.83×10^{-2} wt% min^{-1}. This mean value does not

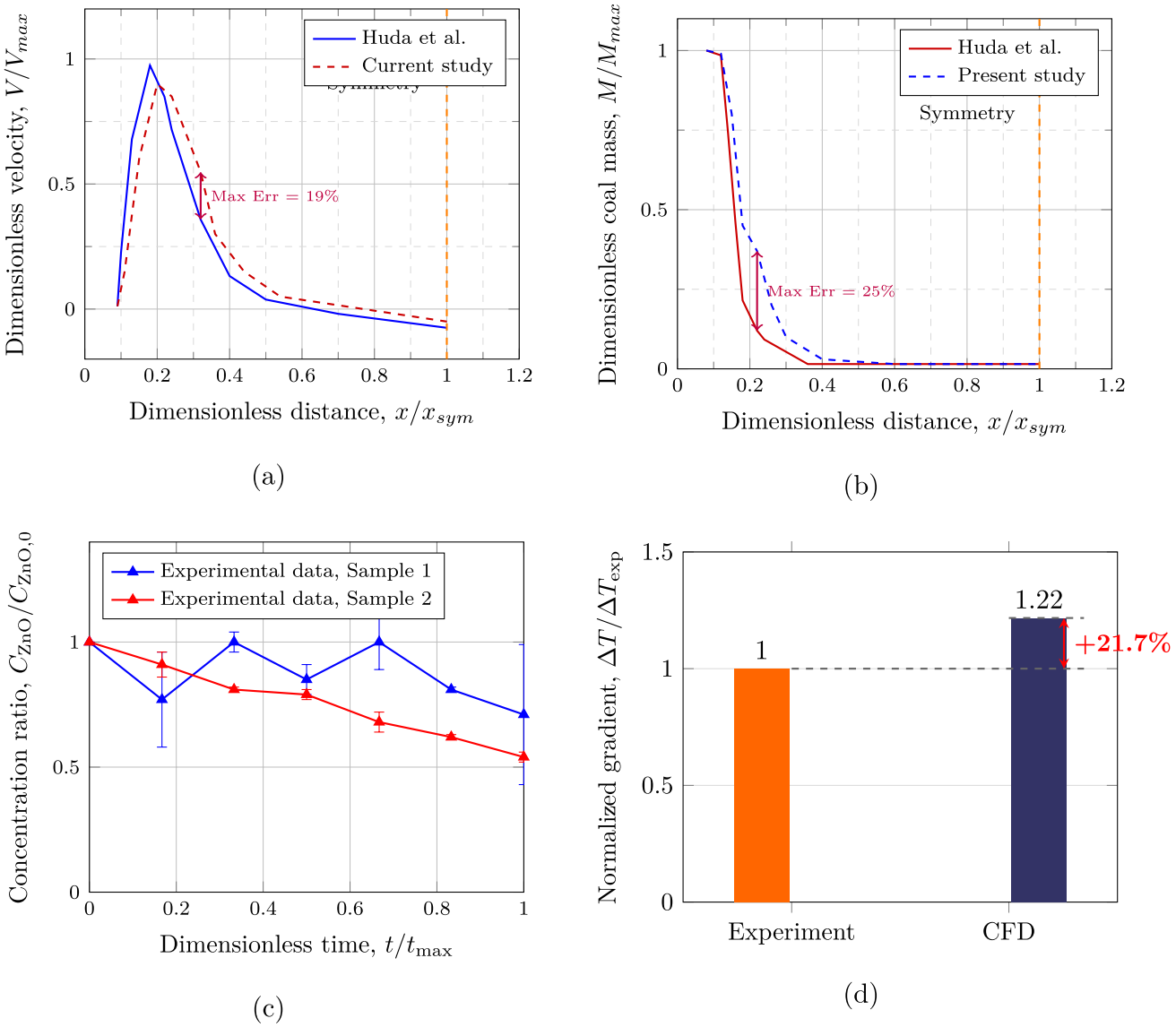

Fig. 5 Verification and partial-validation profiles. **a** Dimensionless vertical velocity along the symmetry line. **b** Normalized coal mass along the symmetry line; panels **a** and **b** are comparisons with the benchmark study of Huda et al. [8]. **c** Normalized experimental ZnO concentration versus dimensionless time for two samples, from Boliden furnace. **d** Normalized cooling-system temperature gradient, $\Delta T/\Delta T_{exp}$, comparing CFD with the experimental baseline

imply that ZnO is consumed at a constant rate. The smallest interval decrease is approximately 0.12 percentage points between 771 and 1029 s, whereas the largest is approximately 0.41 percentage points between 1286 and 1543 s.

The corresponding depletion-rate magnitudes differ by a factor of approximately 3.4, demonstrating that the ZnO response is temporally nonuniform despite the nearly linear appearance of the complete curve. A descriptive linear regression through the plotted values gives $R^2 \approx 0.991$; however, this agreement should not be interpreted as evidence of zero-order kinetics or as a validated reaction-rate expression.

The variation in the interval depletion rate indicates that ZnO consumption is governed by the evolving thermochemical and hydrodynamic state rather than by ZnO concentration alone. Local temperature and CO availability set the chemical driving force, while gas holdup, the bubble-size distribution, and the resulting interfacial area set the contact over which it acts. Turbulent transport couples the two. The comparatively weak decrease near the middle of the cycle, followed by faster depletion during the final third, is not consistent with a simple concentration-controlled first-order response, for which the absolute consumption rate would generally decrease as ZnO becomes depleted.

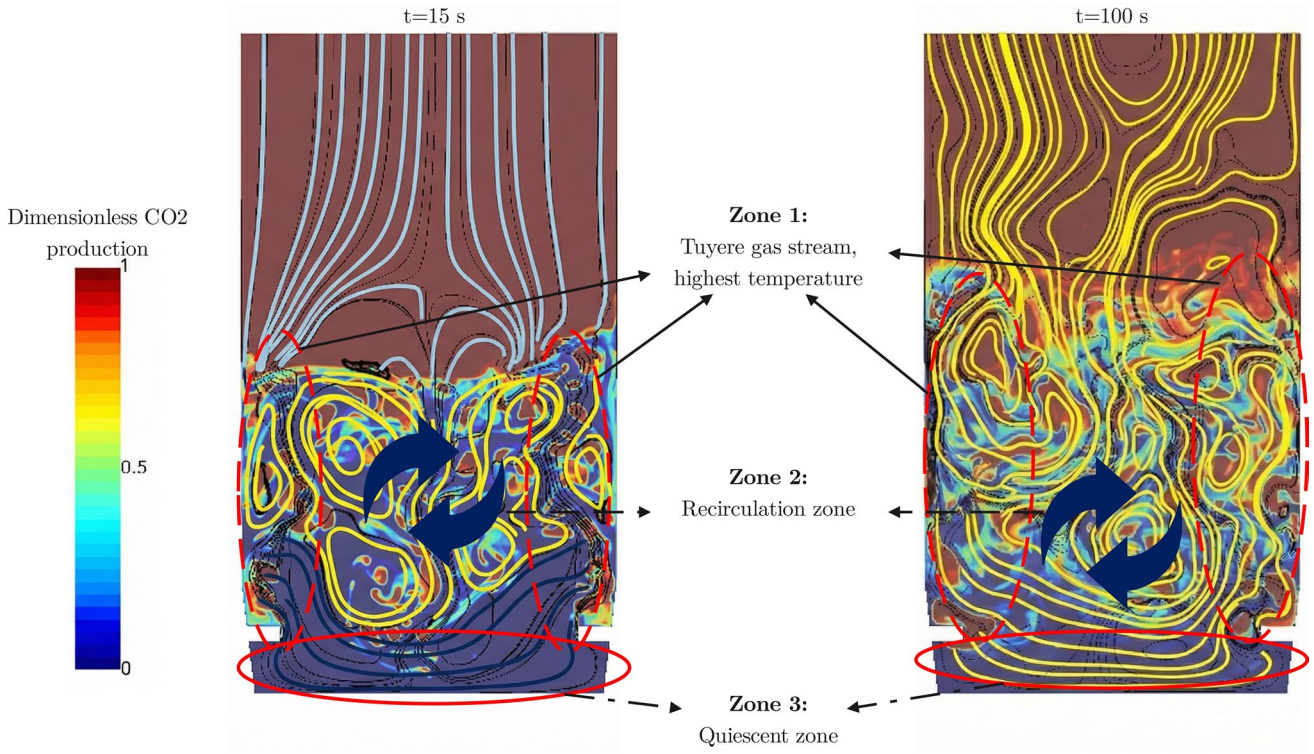

Fig. 6 Instantaneous streamlines and normalized local CO_2 source at $t = 15$ s and $t = 100$ s. The source in each panel is normalized by that panel's instantaneous domain maximum. Color levels therefore indicate the relative spatial distribution and cannot be used to compare absolute source magnitudes between the two times. Regions Z1–Z3 are qualitative descriptive zones rather than quantitatively segmented control volumes

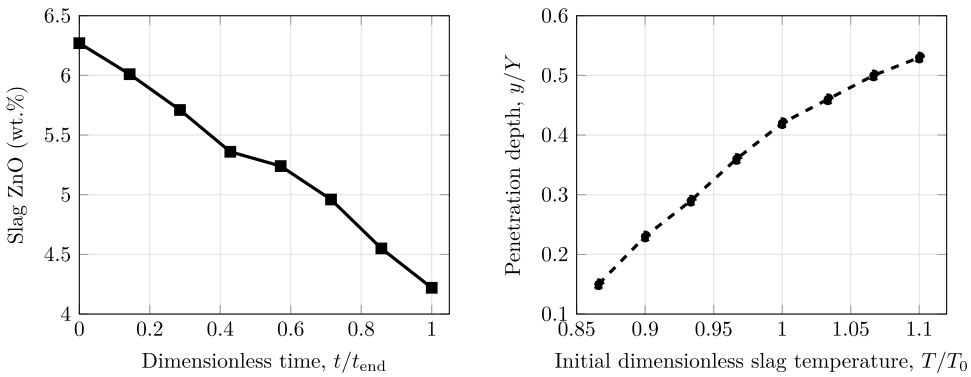

Fig. 7 Reported post-processed trends: **a** slag-phase ZnO concentration over the 1800 s cycle, plotted against t/t_{end}, and **b** dimensionless penetration depth as a function of initial normalized slag temperature. The averaging basis in panel **a** and the case-selection and penetration definitions in panel **b** are stated in the text. Lines connect the plotted points and do not denote validated correlations

The later acceleration cannot be attributed to a rising bath temperature. The largest interval decrease occurs between 1286 and 1543 s, which overlaps the interval over which the mass-weighted slag temperature reported in the section "Reaction-Driven Temperature Evolution and Partial Energy Audit" reaches its minimum, and the smallest interval decrease occurs earlier, when the bath is hotter. The model therefore predicts its fastest ZnO removal near its coldest bath state.

This inversion is the single most important result to resolve before the present mechanistic interpretation can be sustained. The candidate explanations that remain are an increase in local CO availability, an increase in interfacial-area concentration through bubble breakup, and improved spatial overlap between CO-rich gas and ZnO slag; a numerical cause also cannot be excluded. The reported 32.7% decrease is also a concentration-based depletion index and should not automatically be reported as zinc recovery. It is equivalent to the inventory-based ZnO conversion only

when the total slag mass remains effectively constant. If zinc volatilization, reduction of other oxides, phase transfer, or boundary fluxes alter the slag mass, the total ZnO inventory must be evaluated directly. Internal recirculation may redistribute ZnO and modify local concentration gradients, but it cannot independently reduce the globally integrated ZnO mass.

Figure 7b shows a monotonic increase in dimensionless penetration depth as the initial normalized slag temperature rises from $T/T_0 \approx 0.867$ to 1.10, with the remaining operating and injection conditions held fixed. Over this interval, y/Y increases from approximately 0.15 to 0.53, giving an absolute increase of 0.38 and a maximum-to-minimum ratio of approximately 3.53. The penetration predicted at the highest investigated temperature is therefore approximately 253% greater than that obtained at the lowest temperature. Using the reference temperature $T_0 = 1500\,K$, the investigated range corresponds to approximately 1300–1650 K, with consecutive cases separated by about 50 K. The lower temperatures may be subliquidus for representative zinc-fuming slags, leading to fayalite and spinel crystallization and a sharp increase in apparent viscosity. Near cooled furnace walls, this may produce a protective freeze lining with substantial thermal resistance [27–29]. Because solidification and melting were neglected, the low-temperature cases represent a fully liquid approximation and should be interpreted cautiously.

The intermediate penetration values are approximately 0.23, 0.29, 0.36, 0.42, 0.46, and 0.50 at $T/T_0 = 0.90$, 0.933, 0.967, 1.00, 1.033, and 1.067, respectively. At the reference temperature, the plume penetrates to approximately 42% of the normalization length Y. Decreasing the slag temperature by 10%, from $T/T_0 = 1.00$ to 0.90, reduces y/Y from 0.42 to 0.23, corresponding to a reduction of approximately 45.2%. Increasing the temperature by 10%, from $T/T_0 = 1.00$ to 1.10, increases y/Y from 0.42 to 0.53, corresponding to an increase of approximately 26.2%. The response is asymmetric, so the penetration–temperature relationship is nonlinear across the range investigated. Three qualifications apply.

The penetration y is defined as the maximum horizontal distance from the tuyere exit to the connected $\bar{\alpha}_g = 0.5$ isocontour of the time-averaged gas-volume-fraction field, evaluated over the quasi-steady interval of each case. This operational definition represents the mean gas-rich jet region and is subject to the selected volume-fraction threshold. Since the tuyeres are horizontal, y/d_t is used as the principal jet-scale normalization, while y/L_h, where L_h is the horizontal distance from the tuyere exit to the furnace centerline, indicates the fraction of the available bath width reached by the jet. On these horizontal scales the same sweep gives $y/d_t = 2.5$ to 8.8 for $d_t = 0.09$ m, and $y/L_h = 0.19$ to 0.68 for $L_h = 1.17$ m, corresponding to $y = 0.23$ m to 0.80 m. The ratio y/Y, based on the vertical slag depth, is retained only for comparison with the original presentation, and it is a vertical length scale applied to a horizontal distance, so the horizontal normalizations above are the physically appropriate ones.

The abscissa of Fig. 7b is the initial uniform bath temperature of each case, not the bath temperature during the quasi-steady interval over which penetration was measured. The lowest-temperature cases are likely subliquidus for the slag considered; however, the exact liquidus depends on composition and oxygen potential and must be established by a corresponding phase-equilibrium calculation. The fully liquid Newtonian closure is therefore not physically complete in this range. Quantitative interpretation is restricted to cases above the calculated liquidus, whereas the lower-temperature cases are treated only as numerical sensitivity cases.

The positive temperature dependence is physically consistent with the implemented slag-property closure. As the slag temperature increases, the predicted dynamic viscosity generally decreases, reducing viscous momentum dissipation and allowing the injected multiphase plume to retain its momentum over a greater distance. Temperature-dependent changes in slag density and surface tension may also modify hydrostatic resistance, interphase drag, bubble deformation, breakup, and coalescence. The limitations of the two-dimensional representation are stated in the section "Modeling Limitations."

Figure 8 compares the measured normalized slag viscosity [7] with two CFD-based property representations: a temperature-only closure and a closure incorporating both temperature and composition. The horizontal axis decreases from $T^* \approx 1.045$ to 0.900; movement from left to right therefore represents cooling from approximately 1568 to 1350 K for $T_0 = 1500$ K. Across this interval, the measured value of $\mu/\mu_{\max,\mathrm{meas}}$ increases from approximately 0.06 to 1.00, corresponding to a viscosity increase by a factor of about 16.7. The logarithmic ordinate is appropriate for displaying this variation of more than one order of magnitude, although equal vertical distances represent multiplicative rather than additive changes. Both CFD curves reproduce the monotonic increase and agree most closely with the measurements over approximately $0.97 < T^* < 1.02$, where the normalized viscosity increases from roughly 0.09 to 0.20. The temperature-only representation nevertheless shows systematic departures near the limits of the investigated range. It overpredicts the low-viscosity measurements at the highest temperatures and underpredicts several measurements as the slag cools below $T^* \approx 0.96$, where the measured temperature dependence becomes considerably steeper [7].

The maximum absolute error consequently decreases from 47.1 to 22.2%, a reduction of 24.9 percentage points, or approximately 52.9%. The complete signed-error span

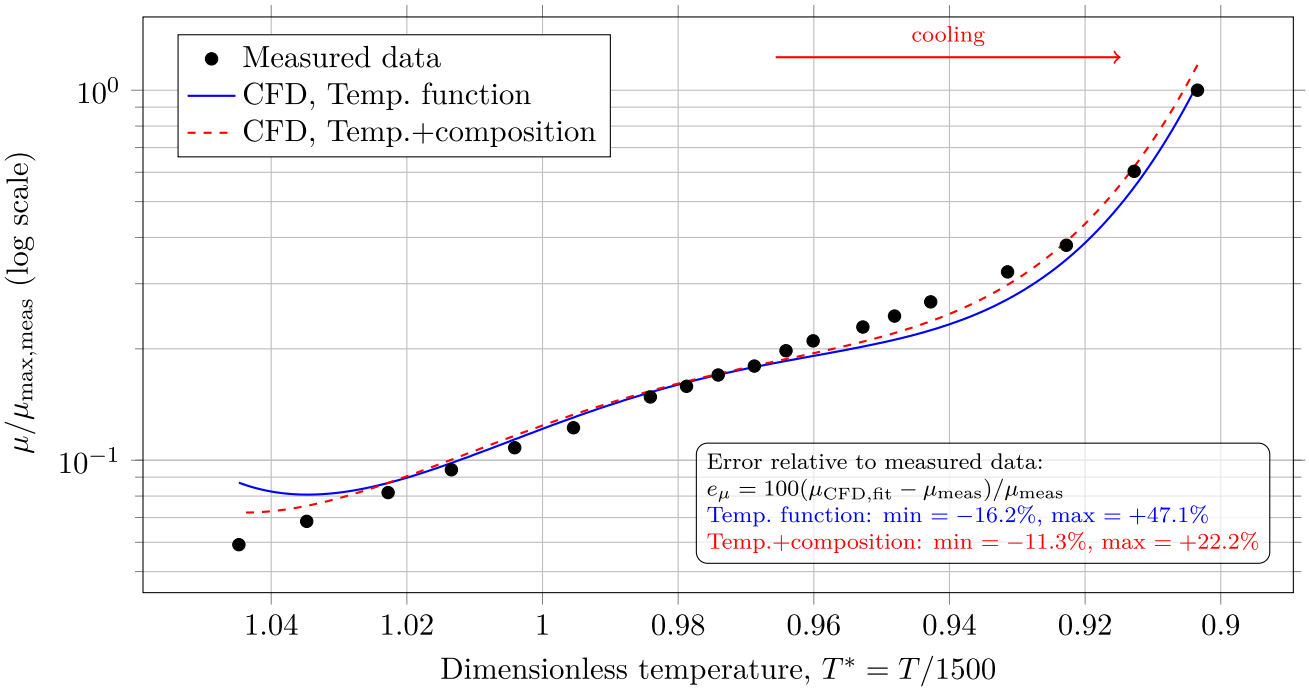

Fig. 8 Normalized viscosity comparison on a logarithmic scale. The CFD curves are represented by fourth-order polynomial fits in logarithmic space. The reported error range is calculated relative to the measured data at the same dimensionless temperature points [7]. The abscissa decreases from left to right, so the slag cools toward the right-hand side. The quoted errors are those of the fitted curves

Table 6 Partial comparison of energy source terms per unit carbon equivalent

Process	CFD (MJ/$kg_{C,eq}$)	Reference (MJ/$kg_{C,eq}$)	δ_i (%)
$C(s) + O_2(g) \rightarrow CO_2(g)$	+32.76	+32.81	−0.15
Air sensible heating (500K → 1500K)	−11.57	−11.59	+0.17
$ZnO(slag) + CO(g) \rightarrow Zn(g) + CO_2(g)$	−3.21	−4.40	+27.05

Positive values denote heat release, whereas negative values denote heat demand, which is the opposite of the convention used in Table 4. This comparison does not constitute a complete furnace energy balance; the signed relative difference is defined as $\delta_i = 100(Q_{i,\mathrm{CFD}} - Q_{i,\mathrm{ref}})/|Q_{i,\mathrm{ref}}|$. A positive value therefore indicates that the CFD term is algebraically greater than the corresponding reference value. No subtotal is reported: iron-oxide reduction is a major endothermic sink in the reference model and is excluded from the present baseline, so a subtotal formed by omitting it from both sides would not compare the same system

also decreases from 63.3 to 33.5 percentage points, that is, the span narrows to about 53% of its original width. Over the same 19 measurement points, the mean absolute percentage error decreases from 20.6 to 15.0%, the values quoted in the abstract. These results indicate that the composition-dependent terms modify the predicted temperature sensitivity in a direction that is more consistent with the measurements, particularly at the high-temperature end and through the rapid viscosity increase below $T^* \approx 0.96$. Two qualifications apply to this improvement. First, both error ranges are evaluated from the fourth-order polynomial fits plotted in Fig. 8 rather than from the closure as implemented in the solver.

The rheological feedback loop introduced in the "Introduction" section operates in both directions here: lower viscosity improves mixing, plume penetration, and gas–slag mass transfer, and therefore the integrated ZnO-reduction rate, while ZnO reduction consumes heat and changes composition, which increases viscosity again. Progressive removal of ZnO and reduction of iron oxides can also alter the relative proportions of network-forming and network-modifying oxides, although the structural effect of ZnO depends on the complete slag composition.

Reaction-Driven Temperature Evolution and Partial Energy Audit

Table 6 provides a partial thermochemical audit of selected energy source terms involved in slag fuming, expressed on

a common basis of 1 kg of carbon equivalent. This normalization permits direct comparison between processes with different reactants and stoichiometric scales, but it should not be interpreted as the total energy associated with 1 kg of slag or with the complete furnace batch. It also does not imply that every unit of injected carbon undergoes all four listed reactions. The actual furnace contribution of each term depends on the carbon feed rate, fixed-carbon fraction, air-to-carbon ratio, reaction extent, local species availability, and duration of operation. Within the CFD model, these terms act at different locations and times. Carbon oxidation is concentrated in oxygen-rich regions close to the tuyeres and within the reacting plume; sensible heating of the injected air occurs as the gas approaches the bath temperature; ZnO reduction occurs where CO-rich gas contacts ZnO slag; and the water–gas reaction occurs where steam reaches sufficiently hot carbonaceous particles.

The oxidation of carbon to CO_2 is the dominant listed heat source, contributing +32.76 MJ/kg of carbon equivalent in the CFD calculation, compared with +32.81 MJ/kg of carbon equivalent in the reference calculation. The difference is only −0.05 MJ/kg, or −0.15%, indicating close consistency in the enthalpy assigned to complete carbon oxidation. In an operating SFF, however, carbon may initially undergo partial oxidation to CO, followed by subsequent CO oxidation or participation in oxide reduction. The tabulated reaction should therefore be interpreted as the thermochemical contribution associated with the specified overall carbon-to-CO_2 pathway, rather than evidence that all injected carbon reacts directly to CO_2 at the tuyere. Heating the injected air from 500 to 1500 K requires 11.57 MJ/kg of carbon equivalent in the CFD calculation. The air-heating term implies a specific blast ratio, and that ratio can be checked. Heating air from 500 to 1500 K takes 1133 kJ/kg. The tabulated 11.57 MJ/kg of carbon therefore corresponds to 10.2 kg of heated gas per kilogram of carbon. Complete combustion of pure carbon requires 11.5 kg of air per kilogram, so the blast is at 89% of that value.

This ratio is expected, not anomalous. The overall C/CO_2 pathway provides the largest potential chemical heat release: the dominant term in Table 6 is carbon to CO_2 at 32.8 MJ/kg of carbon oxidation. Partial oxidation to CO releases only 9.2 MJ/kg and cannot cover the bath heat demand. A blast near complete-combustion stoichiometry is therefore the normal operating point for this process.

The global ratio also says nothing about the oxygen potential at the reaction sites. Oxygen is consumed within a few tuyere diameters of the injection point. CO burns higher in the plume and in the freeboard. The bath interior and the interiors of the rising bubbles, where ZnO is reduced, stay CO-rich.

The ZnO-reduction term is the most important source of disagreement. The CFD model assigns a heat demand of −3.21 MJ/kg of carbon equivalent to the reaction between slag-phase ZnO and CO, whereas the reference value is −4.40 MJ/kg. The CFD term is therefore 1.19 MJ/kg less negative, giving the reported signed difference of +27.05%. This term is the product of the reaction extent and the reaction enthalpy. If both calculations use the same enthalpy, a heat demand smaller in magnitude by 27% means that the CFD predicts approximately 27% less ZnO reduced than the reference, not merely a smaller thermal sink. The CFD ZnO-reduction demand is equivalent to approximately 9.8% of the listed combustion heat, whereas the reference demand corresponds to approximately 13.4%. This discrepancy is metallurgically significant because ZnO reduction is the principal fuming reaction and directly couples zinc removal to bath cooling. A smaller endothermic source may lead to a higher predicted local temperature, lower calculated slag viscosity, deeper plume penetration, stronger recirculation, and enhanced gas–slag mass transfer.

Figure 9a shows that the CFD and reference models start from the same normalized slag temperature, $T/T_0 = 1.00$, but subsequently predict markedly different transient responses. The reference curve is the kinetic process model of Richards and Brimacombe [4]. The CFD curve rises rapidly to approximately 1.13 at $t/t_{end} = 0.10$ and reaches a maximum of about 1.16 at $t/t_{end} = 0.20$. By comparison, the reference increases only gradually to approximately 1.04 over the same interval. Taking the vertical markers at $t/t_{end} \approx 0.25$ and 0.83 as stage boundaries, the CFD result comprises an initial heating period, a prolonged cooling period, and a final partial thermal recovery. After the first marker, the CFD temperature decreases from approximately 1.15 to 1.00 at $t/t_{end} = 0.50$, before reaching a minimum of approximately 0.89–0.90 between $t/t_{end} = 0.70$ and 0.80. It then recovers to approximately 0.98 at the end of the cycle. For $T_0 = 1500$ K and $t_{end} = 1800$ s, the CFD maximum corresponds to approximately 1740 K at 360 s, whereas the minimum corresponds to approximately 1335–1350 K between 1260 and 1440 s.

The resulting peak-to-trough temperature excursion is approximately $0.27T_0$. In contrast, the reference result remains within the much narrower range $1.00 \lesssim T/T_0 \lesssim 1.05$ and finishes at approximately 1.04. The CFD model therefore overpredicts the reference temperature by approximately 11–12% near the early maximum, crosses the reference curve at approximately $t/t_{end} = 0.45$–0.48, underpredicts it by approximately 11–12% near the minimum, and remains about 6% lower at the end of the cycle [4]. The predicted excursion of 405 K over 30 min is also far larger than industrial bath records for this process, and its minimum lies at or below the liquidus of the Table 2 composition, so the late-cycle result falls outside the validity range of every property closure in Table 5.

The discrepancy is not distributed randomly: the CFD model is systematically hotter during the initial stage and

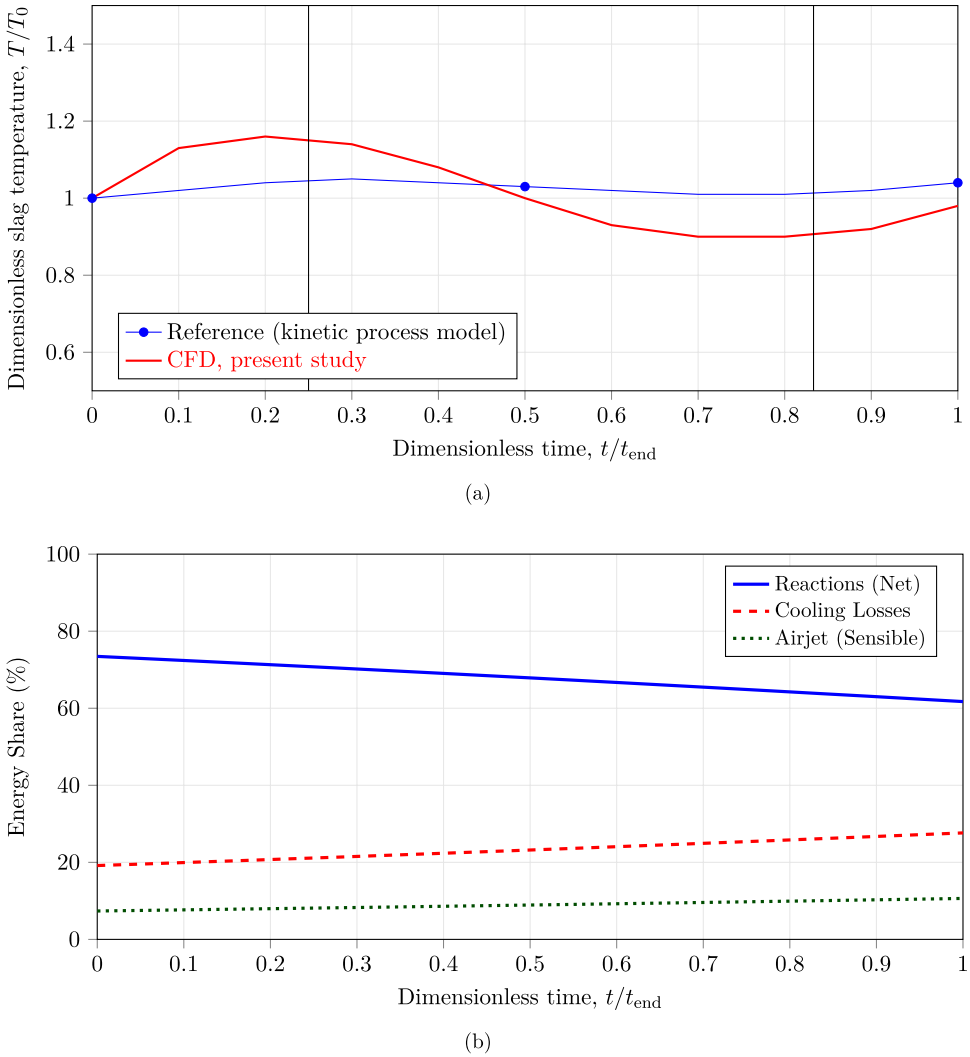

Fig. 9 Combined thermal analysis: **a** temporal evolution of slag temperature and **b** variation in energy shares over dimensionless time. In panel **b** the three curves are normalized by the sum of the absolute magnitudes of the three terms and therefore sum to 100% at every instant

systematically colder during most of the later cycle. The early CFD overshoot is consistent with rapid local heat release from carbon oxidation and associated gas-phase reactions exceeding the simultaneous sensible-heating demand, endothermic reduction demand, and external heat losses. The subsequent temperature decline indicates that the balance between heat generation, endothermic chemistry, gas heating, and cooling losses changes as fuming progresses. Differences between the two curves may also arise because the reference model represents a spatially aggregated state, whereas the CFD model resolves finite-rate reactions, local species availability, plume transport, thermal gradients, and delayed redistribution of heat throughout the slag bath. The physical interpretation also depends on how the CFD temperature was averaged; a slag-mass-weighted temperature is generally more suitable for an energy analysis than a simple volume average, particularly when density and phase fraction vary, and the basis used in Fig. 9a. Furthermore, T/T_0 is not directly proportional to stored sensible energy because the instantaneous slag mass and heat capacity may change with temperature and composition [15].

Figure 9b quantifies the progressive redistribution of the reported thermal contributions. All three curves are normalized at each instant by the sum of the absolute magnitudes of the three terms, so they sum to 100% by construction; the two sinks are plotted as positive magnitudes, and the figure is therefore a set of relative magnitudes and not a signed energy balance. The net-reaction share decreases from approximately 73.5% at $t/t_{\text{end}} = 0$ to approximately 61.7% at $t/t_{\text{end}} = 1$, corresponding to a decrease of about 11.7 percentage points, or approximately 16% relative to its initial value. Over the same interval, the cooling-loss share increases from approximately 19.2 to 27.6%, an increase of 8.5 percentage points or approximately 44%, while the sensible-heating share associated with the air jet increases from approximately 7.4 to 10.6%, an increase of 3.3 percentage points or approximately 44%. The combined share of the two thermal sinks consequently increases from approximately 26.5 to 38.3%.

The ratio of the net-reaction contribution to the combined sink contribution therefore decreases from approximately 2.8 at the beginning to 1.6 at the end. This reduction indicates a substantial contraction of the relative thermal margin available from the reacting system. The net-reaction term is the algebraic sum of the exothermic carbon and CO oxidation rates and the endothermic ZnO-reduction and Boudouard rates; the water–gas and carbon–steam reactions contribute nothing in the baseline because no H_2O enters the represented system [16].

The decreasing reaction-to-sink ratio is qualitatively consistent with the decline in CFD temperature after $t/t_{\mathrm{end}} \approx 0.20$, but the energy shares alone cannot determine the direction or rate of temperature change. Temperature is governed by the absolute signed heat rates, their time integral, the thermal capacity of the slag and refractory, and enthalpy transport through the system boundaries. An increasing percentage assigned to cooling does not necessarily mean that the absolute cooling power increases. Because radiative and convective losses depend on the slag, freeboard, wall, and refractory temperatures, their absolute magnitude could decrease during bath cooling while their percentage rises because the total reaction power decreases more rapidly. The same distinction applies to air-jet sensible heating: for constant air flow and inlet temperature, a lower bath temperature may reduce the absolute heating duty even though its relative share increases.

Bubble-Scale Estimates and PBM Distribution

The temperature and composition dependence of slag viscosity is described in the section "Zinc Depletion, Jet Penetration, and the Slag-Viscosity Closure" and is not repeated here. Two consequences matter for the bubble population. Higher viscosity increases drag on rising bubbles, delays gas disengagement, and can promote bubble entrapment, foaming, or slopping, depending on gas rate, slag chemistry, surface tension, and hydrodynamics.

Figure 10 illustrates the computed residence time, t_{res}, as a function of bubble diameter within a characteristic interaction layer of $H = 0.5\,\mathrm{m}$, corresponding to the vertical extent of the tuyere plume region. This height is a nominal plume-interaction scale rather than the full rise path: with the tuyeres near the bottom of a 1.5 m bath, the physical rise height is closer to 1.4 m. Every residence time in Fig. 10 and Table 8 scales linearly with H and should be read accordingly. The pronounced nonlinearity of the profile is a direct consequence of the transition between hydrodynamic drag regimes.

In the low Reynolds number limit (Stokes regime), fluid viscosity dominates the flow. Here, the bubble rise velocity is highly sensitive to size ($U_b \propto d_b^2$), which creates a strong inverse relationship for residence time ($t_{\mathrm{res}} \propto d_b^{-2}$). Physically, this means that reducing bubble size strongly slows its ascent in the Stokes limit; for example, halving the diameter quadruples the available gas–liquid contact time.

In contrast, at higher Reynolds numbers (inertial regime), the flow physics change as the drag coefficient stabilizes near a constant value. In this region, the rise velocity increases more gradually ($U_b \propto d_b^{1/2}$), which significantly weakens the sensitivity of residence time to diameter ($t_{\mathrm{res}} \propto d_b^{-1/2}$). This hydrodynamic distinction highlights a critical modeling constraint: assuming a constant slip velocity introduces a systematic bias in residence-time calculations, particularly within the 1–10 mm transitional range relevant to the current furnace conditions. The volumetric rate of zinc fuming, $\dot{r}_{\mathrm{Zn}}$, is governed by the heterogeneous nature of the gas–slag reaction. Unlike homogeneous combustion, reduction of dissolved ZnO occurs at gas–slag interfaces; consequently, the overall fuming rate scales with the available interfacial area density, a, together with the local mass-transfer and kinetic driving forces. In the limiting case of mass-transfer control with approximately constant driving force, $\dot{r}_{\mathrm{Zn}} \propto k_L a$, where k_L is an effective liquid-side mass-transfer coefficient.

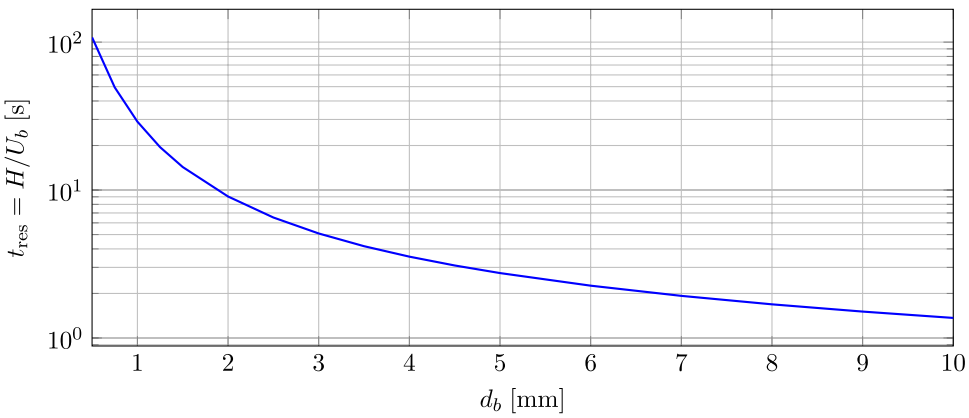

Fig. 10 Bubble residence time over the representative interaction height $H = 0.5\,\mathrm{m}$ as a function of bubble diameter. Residence times scale linearly with H

Control of the bubble size distribution is therefore as consequential as the thermodynamic driving force for reduction. For a dispersed gas phase, the interfacial area per unit gas volume scales inversely with the Sauter mean diameter, $a_v = 6/d_{32}$, so a reduction in bubble size yields a hyperbolic growth of the reaction surface available per unit gas volume. This geometric amplification increases the volumetric mass-transfer conductance $k_L a$. The d_{32}^{-1} growth of the area term dominates the weaker, regime-dependent size sensitivity of the film coefficient k_L, and the CO contacts the slag interface over a larger cumulative area within its finite residence time in the bath. Enhanced interfacial transport does not, however, establish that the system passes into a purely kinetically controlled regime [30, 31]. In a resistance-in-series description, the intrinsic heterogeneous kinetics at the gas–slag interface, the evolving CO/CO_2 composition of the rising gas, the finite bubble residence time, and the local oxygen potential of the melt can each still limit the utilization efficiency of the reductant inventory. In particular, as reduction proceeds, the gas approaches the CO/CO_2 ratio in equilibrium with the local oxygen potential, and this thermodynamic ceiling bounds the attainable utilization independently of the interfacial area [12]. Table 7 summarizes the two asymptotic drag regimes that govern bubble rise in viscous slag [23, 32] and the resulting residence-time scaling for a fixed interaction height H.

This extension of residence time is directly coupled to metallurgical performance through the fuming rate, $\dot{r}_{Zn}$. Since CO-mediated zinc-oxide reduction is a heterogeneous interface reaction, the extent of conversion depends on both the instantaneous interfacial rate and the available gas–slag contact time. Increasing t_{res} increases the relevant Damköhler number when the characteristic transport/residence time becomes large compared with the characteristic chemical or interfacial mass-transfer time.

In the inertia-dominated regime, bubbles can traverse the interaction layer with incomplete utilization of the reductant inventory, particularly if CO transfer or ZnO transport through the slag-side boundary layer is limiting. Representative small-diameter estimates using the same local-viscosity basis are summarized in Table 8.

This table demonstrates the pronounced sensitivity of submillimeter bubble motion to diameter under the adopted viscous-flow conditions. The tabulated diameters lie below the modal sizes of the predicted bubble population and are therefore analytical bounds that illustrate the leverage of size control, not sizes returned by the simulation. Increasing the bubble diameter from 0.10 to 0.20 mm increases the terminal rise velocity from 1.91×10^{-4} to $7.63 \times 10^{-4}\ m/s$, corresponding to a fourfold increase, while the residence time over the 0.5 m interaction height decreases from approximately 2620 to 655 s. The available gas–slag contact time is therefore reduced by approximately 75% when the diameter is doubled. Increasing the diameter further to 0.50 mm increases the rise velocity to $4.77 \times 10^{-3}\ m/s$, which is 25 times the value calculated for the 0.10 mm bubble, and reduces the corresponding residence time to only 105 s, or 1.75 min. Relative to the smallest bubble, this represents a 96% reduction in contact time. The Reynolds number increases by a factor of approximately 125, from 6.68×10^{-4} to 8.35×10^{-2}, but remains well below unity throughout the tabulated range. The motion is therefore still dominated by viscous resistance rather than wake inertia, supporting the creeping-flow basis used for these estimates. The increase in diameter does not produce a proportional change in residence time; even a moderate increase in bubble size causes a substantial acceleration of gas disengagement from the slag [33].

The metallurgical significance of this diameter dependence extends beyond residence time. At a fixed gas volume, reducing the diameter from 0.50 to 0.10 mm produces approximately five times more gas–slag surface area while simultaneously increasing the calculated residence time by a factor of 25. Under otherwise unchanged conditions, this combination corresponds to a nominal 125-fold increase in interfacial area–time exposure per unit gas volume. Each fine bubble therefore acts as a mobile reaction site. Reduction occurs within this thin interfacial region, after which Zn

Table 8 Stokes-limit terminal velocities, residence times, and Reynolds numbers for submillimeter isolated bubbles over $H = 0.5$ m

d_b [mm]	U_b [m/s]	t_{res} [s]	t_{res} [min]	Re
0.10	1.91×10^{-4}	2.62×10^{3}	43.7	6.68×10^{-4}
0.20	7.63×10^{-4}	6.55×10^{2}	10.9	5.34×10^{-3}
0.50	4.77×10^{-3}	1.05×10^{2}	1.75	8.35×10^{-2}

The calculation uses $U_b = (\rho_\ell - \rho_g) g d_b^2/(18\,\mu)$, $\rho_\ell = 3500\,\mathrm{kg/m^3}$, negligible ρ_g, and $\mu = 0.10$ Pa s

Table 7 Asymptotic bubble-drag regimes and residence-time scaling for a fixed interaction height

Regime	Condition	Rise-velocity scaling	Residence-time scaling
Viscous limit	$\mathrm{Re} \ll 1$	$U_b \propto d_b^2$	$t_{res} \propto d_b^{-2}$
Approximate form-drag limit	$C_D \approx$ constant	$U_b \propto d_b^{1/2}$	$t_{res} \propto d_b^{-1/2}$

These limits are analytical reference behaviors, not separate CFD results

vapor and CO_2 are transferred into the gas phase and carried away from the reaction site. Heat must also be supplied locally because zinc volatilization is endothermic (Table 4). Hydrodynamics, species transport, conversion, and heat transfer are thus coupled across one thin surface [34].

The 0.10 mm bubble has a calculated residence time of 43.7 min, which exceeds the nominal 30 min fuming cycle. This result should not be interpreted as evidence that an individual bubble remains intact for the entire calculated period. It indicates that buoyancy-driven slip alone would be insufficient to transport such a small bubble through the assumed 0.5 m layer within one cycle. In the furnace, its actual lifetime and trajectory would also depend on plume recirculation, turbulent dispersion, gas holdup, bubble–bubble interaction, coalescence, breakup, thermal expansion, and spatial variations in slag viscosity. Long residence time also does not guarantee complete ZnO conversion. The benefit is realized only while the bubble retains sufficient CO, the surrounding slag supplies dissolved ZnO, the interface remains at a favorable temperature and oxygen potential, and the reaction products are removed rapidly enough to preserve the local driving force. Table 8 should therefore be interpreted as an indication of the sensitivity of contact time to bubble size. It predicts neither bubble lifetime nor zinc recovery in a turbulent plume.

Table 9 shows that the gas-volume distribution does not determine the gas–slag interfacial area directly. The fine component contains only 23.1% of the total gas volume, but its inverse-diameter moment, $E_i[d^{-1}] = 0.5462\ \mathrm{mm}^{-1}$, is approximately 4.4 times that of the coarse component. After weighting by volume fraction, the fine population contributes $0.1262\ \mathrm{mm}^{-1}$ to the interfacial-area indicator, compared with $0.0945\ \mathrm{mm}^{-1}$ for the coarse population. It therefore provides 57.2% of the estimated total interface, despite the coarse bubbles accounting for 76.9% of the gas volume. The fine-bubble contribution is approximately 34% greater than that of the coarse population.

The gas–slag interface described above is therefore the controlling surface for the fuming process. Bubble coalescence can reduce this reactive area substantially even when the total gas volume remains unchanged, whereas breakup and sustained fine-bubble dispersion increase the number of available reaction sites. The reported area shares are distribution-based estimates rather than direct reaction-rate measurements; their metallurgical effect also depends on local temperature, CO concentration, liquid-side mass transfer, residence time, and interfacial reaction kinetics.

The bubble size distribution in Fig. 11 exhibits two distinct modes associated with different gas sources. The narrower mode near $d \approx 1.70$ mm corresponds to

Table 9 Estimated gas-volume and interfacial-area contributions of the two fitted size-distribution components

Component	ϕ_i	$\mathbb{E}_i[d^{-1}]\,(\mathrm{mm}^{-1})$	$\phi_i\mathbb{E}_i[d^{-1}]\,(\mathrm{mm}^{-1})$	Area share (%)
Fine component	0.231	0.5462	0.1262	57.2
Coarse component	0.769	0.1229	0.0945	42.8
Total	1.000	–	0.2207	100.0

Here, ϕ_i is the component volume fraction and $\mathbb{E}_i[d^{-1}]$ is its inverse-diameter moment; The interfacial-area share of component i is calculated as $\phi_i\mathbb{E}_i[d^{-1}]/\sum_j \phi_j\mathbb{E}_j[d^{-1}]$

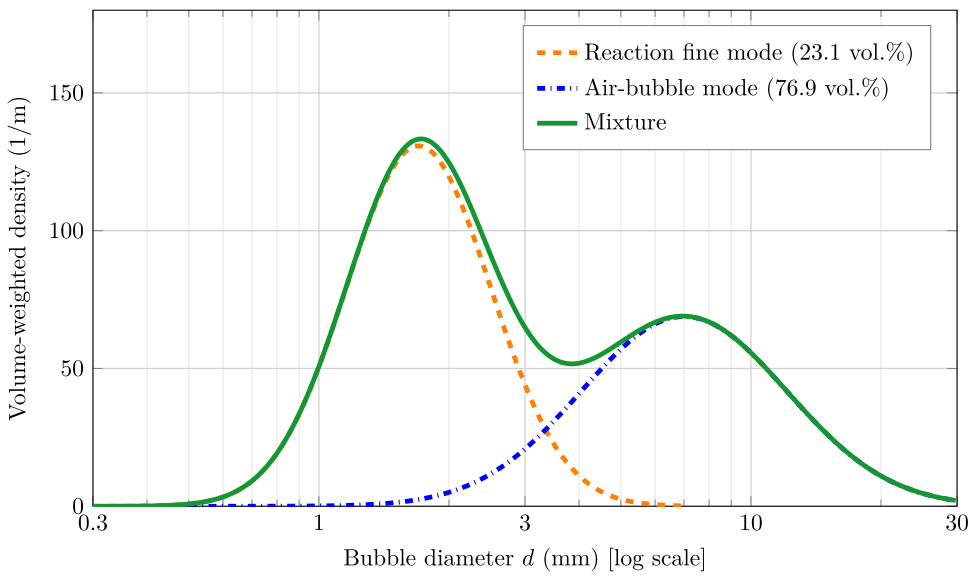

Fig. 11 Illustrative volume-weighted bubble-size distribution at $t = 30$ min. The component curves are plotted with the same modal weights

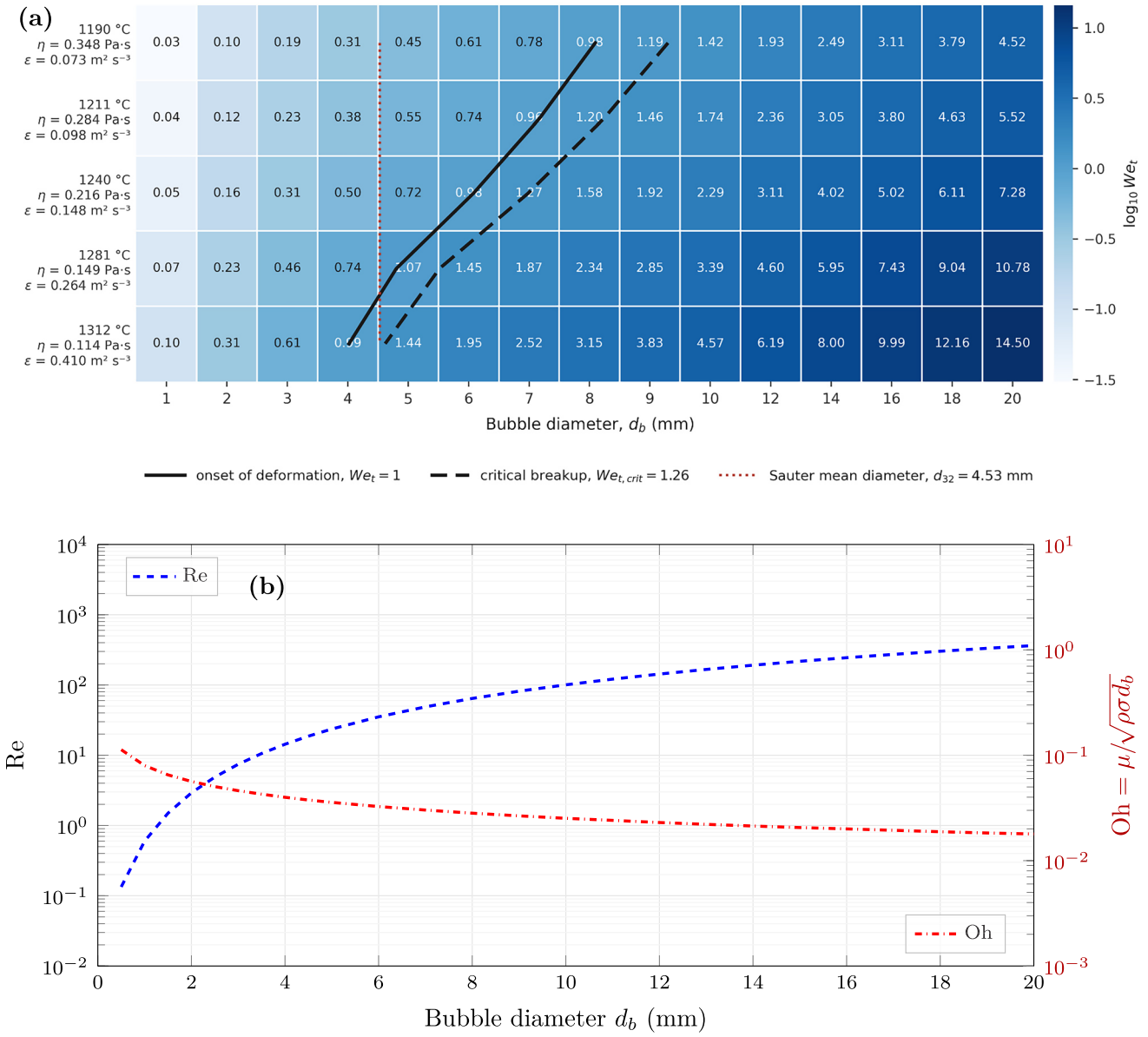

Fig. 12 Dimensionless analysis of bubble hydrodynamics: **a** variation of Weber number with bubble diameter for $\mu = 0.075$–0.25 Pa s; **b** evolution of Reynolds and Ohnesorge numbers for the single reference state $\mu = 0.10$ Pa s, $\rho_\ell = 3500$ kg/m^3, $\sigma = 0.45$ N/m

reaction-generated gas, whereas the broader mode near $d \approx 7.00$ mm corresponds to injected air bubbles whose size is governed by the balance between turbulent breakup and coalescence. For visualization in Fig. 11, each mode is fitted with a log-normal profile ($\sigma_{\ln d} \approx 0.385$ for the fine-bubble mode and 0.548 for the coarse mode); however, explicit first-principles nucleation is not resolved in the present PBM, and the emergence of these modes reflects the specified gas source terms together with the adopted breakup/coalescence closures rather than a mechanistic nucleation model.

The green mixture curve represents the combined total of the two fitted, volume-weighted modes. The dip observed near $d \approx 3.5$ mm is therefore an interpretive feature of the fitted bimodal representation, not direct evidence of a separately resolved coalescence threshold. Although the fine-bubble mode accounts for only 23.1% of the total gas volume, its smaller characteristic diameter gives a disproportionately large interfacial-area contribution. Using the two representative modes in Fig. 11, $d_f \approx 1.70$ mm and $d_c \approx 7.00$ mm, the area fraction estimated from $(\phi_i/d_i)/\sum_j(\phi_j/d_j)$ is approximately 55.3% for the fine-bubble mode.

Figure 12a shows the adopted critical value $We_{t,crit} = 1.26$. Slag density and interfacial tension are taken as 3263–3300 kg/m^3 and 0.390–0.400 N/m over the temperature range considered, and the slag viscosity in each row of Fig. 12a is evaluated from the correlation mentioned above.

As the bath temperature increases from 1190 to 1312 °C, the slag viscosity falls from 0.348 to 0.114 Pa s, and the dissipation rate rises from 0.073 to 0.410 m^2/s^3. Over that range the diameter corresponding to $We_t = 1$ decreases from 8.10 to 4.02 mm, and the diameter corresponding to $We_{t,crit} = 1.26$ from 9.30 to 4.62 mm. Both boundaries therefore shift markedly toward smaller bubble sizes as the slag becomes hotter and less viscous.

At the Sauter mean diameter, $d_{32} = 4.53$ mm, the turbulent Weber number rises from 0.38 at 1190 °C to 1.22 at 1312 °C. The mean bubble thus evolves from a stable regime well below the deformation threshold to a condition close to, but still below, the adopted breakup boundary: at the hottest condition, $We_t = 1.22$ is 0.97 times $We_{t,crit}$, that is, 3.2% below it. A modest further increase in local hydrodynamic stress would bring the mean bubble into the breakup regime.

Breakup over the mapped range is nevertheless governed by the coarse tail of the bubble size distribution rather than by the mean. Bubbles of 4 mm and smaller remain below the deformation threshold at every condition (maximum $We_t = 0.99$). Bubbles of 10 mm and larger exceed the breakup threshold at every condition (minimum $We_t = 1.42$). Between these bounds the behavior is temperature dependent: bubbles of 5–9 mm cross the threshold progressively as the bath heats.

Figure 12b shows how the flow around a rising bubble changes with size in the slag. The curves correspond to a superheated fayalite slag with $\mu \approx 0.1$ Pa s, $\rho \approx 3500$ kg/m^3, and $\sigma \approx 0.45$ N/m. The two curves together give the Weber number, which passes the breakup value of about 12 near $d_b = 13$ mm. Bubbles larger than this fragment as they rise. The bath consequently does not sustain bubbles much above the crossing diameter, which sets the upper limit of the bubble size distribution.

Bubble size matters because the fuming reactions run at the bubble surface [35]. ZnO dissolved in the slag is reduced by CO at the interface, the CO is regenerated inside coal-bearing bubbles by the Boudouard reaction, and part of the CO is lost to reduction of ferric iron. Zinc oxide and ferric iron must diffuse through the slag to the bubble surface, and this liquid-side transport is the slow step over most of the cycle [12]. Smaller bubbles give more surface per unit of injected gas and better CO utilization. Slag viscosity works against this. Losing 100 K of superheat roughly doubles or triples the viscosity, and 20% solid spinel or olivine adds another factor of about 3. The bubbles then rise more slowly, oscillate less, resist breakup, and grow coarser, so the reaction surface per unit gas shrinks. Cold or partly solidified slag therefore fumes poorly through the hydrodynamics alone, before any change in the reaction kinetics at the interface.

Scope Limitations and Excluded Mechanisms

The framework deliberately omits several mechanisms that are present in an industrial SFF. These simplifications were adopted to keep the coupled reacting multiphase model computationally tractable and to isolate the dominant flow, heat-transfer, coal-conversion, and zinc-reduction processes over the full transient cycle. Two groups of assumptions are particularly relevant to the interpretation of the results: the unresolved chemistry, principally the iron-redox reactions discussed in the section "Treatment of Iron Redox Chemistry," and the geometric and numerical approximations associated with the two-dimensional mid-plane representation described in the section "Modeling Limitations." Their implications are therefore stated explicitly, and the conclusions are restricted to the phenomena resolved by the present model.

Treatment of Iron Redox Chemistry

The iron redox family, represented by the $Fe^{2+}/Fe^{3+}/Fe^0$ system, was not explicitly resolved in the present simulation framework. In this work, Fe species were incorporated implicitly through the effective slag composition and thermophysical properties, rather than through a fully coupled transient iron-redox transport model. This modeling choice was made to keep the present study focused on the coupled gas–slag hydrodynamics, heat transfer, and zinc volatilization behavior and because a reliable representation would require oxidation-state-resolved composition data, validated kinetic parameters, and a nonideal thermodynamic slag model.

The exclusion has consequences that should be stated plainly. In fayalitic copper slags, the Fe^{2+}/Fe^{3+} couple buffers the local oxygen potential, competes with ZnO for CO, and influences polymerization and viscosity, so a model without it will tend to overstate the CO available for zinc reduction and understate the damping of the melt response to fluctuations in coal and blast rate. Excessive reduction toward metallic iron is a further operational limit, since metallic prills withdraw iron from the redox cycle and reduce selectivity. A spatially resolved treatment of $Fe^{2+}/Fe^{3+}/Fe^0$ evolution is deferred to a later part of this series.

Modeling Limitations

Several simplifications of the present framework should be considered when interpreting the results. These limitations

do not invalidate the modeling strategy, but they restrict the level of quantitative extrapolation that can be made from the current two-dimensional baseline case.

- The model employs a two-dimensional planar domain. It therefore cannot capture three-dimensional tuyere-plume interaction, lateral recirculation, end-wall effects, swirl-induced asymmetry, or nonuniform gas holdup across the furnace width. A coarse three-dimensional comparison, even if performed with reduced chemistry, is recommended to quantify the error introduced by the mid-plane approximation.
- Freeze-lining formation at the water-cooled walls is not modeled. A freeze lining would modify the local wall heat flux, effective bath geometry, active slag volume, near-wall viscosity, and residence time. Neglecting it can overestimate heat extraction and misrepresent the true liquid domain available for reaction.

Conclusion

This study developed a transient two-dimensional Eulerian–Eulerian CFD framework for an industrial-scale slag-fuming configuration, coupling finite rate oxidation and oxide reduction source terms, an S-Gamma population balance model, and temperature- and composition-dependent slag-property updates. Over a 30-min fuming cycle, the model was used to trace how reaction heat, slag rheology, jet penetration, and the evolving bubble population act on one another through the interfacial area they share. The results support the central conclusion that, within the model, zinc fuming is controlled by coupled heat availability, CO supply, slag-side transport, and gas–slag interfacial area, not by equilibrium thermodynamics alone. In the volume-averaged model, the dispersed gas phase acts as a carrier of momentum, heat, reductant, and interfacial area. Individual bubbles are not resolved as separate reactors; rather, their effect enters through gas holdup, slip velocity, residence time, and PBM-derived d_{32} and a_i. This distinction is important because the predicted fuming rate depends on closure models for breakup, coalescence, drag, mass transfer, and reaction kinetics. The following conclusions can be drawn from the present baseline calculation:

- The predicted ZnO depletion rate varies by a factor of approximately 3.4 across the cycle, and its fastest interval coincides with the coolest bath state. The interval of fastest predicted ZnO depletion coincides with the minimum bath temperature. Increased CO availability, interfacial area, and spatial overlap are plausible explanations, but their relative contributions were not resolved by the diagnostics reported here.
- Tuyere jet penetration increases strongly with the initial bath temperature through the associated viscosity reduction. As T/T_0 rises from 0.867 to 1.10, y/d_t increases from 2.5 to 8.8 and y/L_h from 0.19 to 0.68, corresponding to 0.23 to 0.80 m; against the 1.5 m slag depth the same lengths give $y/Y = 0.15$ to 0.53. The sensitivity exceeds modified-Froude number correlations for round jets, consistent with the two-dimensional slot-jet geometry discussed in the section "Modeling Limitations."
- The interfacial area available for reaction is controlled by the fine end of the bubble population rather than by bulk gas holdup. In the two-mode representation of the injected and reaction-generated gas sources (Appendix section "Population Balance Model: S-Gamma Closure"), the fine mode near $d \approx 1.70$ mm carries 23.1% of the gas volume and approximately 57.2% of the estimated interfacial area. Sustaining this fine mode through bubble breakup is therefore as consequential for zinc removal as the thermodynamic driving force.

Appendix

Species Transport and Finite-Rate Chemistry

Because both the gas-phase composition (CO, CO_2, O_2, Zn(g), N_2, H_2O, H_2, SO_2) and the slag-phase oxide fractions (ZnO, etc.) evolve during fuming, conservation of individual chemical species must be solved alongside the bulk conservation equations [36].

$$\frac{\partial}{\partial t}\left(\alpha_q \rho_q Y_{i,q}\right) + \nabla \cdot \left(\alpha_q \rho_q \mathbf{v}_q Y_{i,q}\right) = -\nabla \cdot \left(\alpha_q \mathbf{J}_{i,q}\right) + \alpha_q R_{i,q} + S_{i,q} + \sum_{p \neq q} \dot{m}_{i,pq}, \tag{21}$$

where $\mathbf{J}_{i,q}$ is the diffusive flux of species i, $R_{i,q}$ is the net chemical production rate, $S_{i,q}$ denotes user-defined source terms (e.g., for prescribed coal partitioning), and $\dot{m}_{i,pq}$ represents interphase transfer of species i from phase p to phase q.

The diffusive flux is modeled using gradient (Fickian) diffusion with a turbulent contribution:

$$\mathbf{J}_{i,q} = -\left(\rho_q D_{i,q} + \frac{\mu_{t,q}}{\mathrm{Sc}_t}\right)\nabla Y_{i,q}, \tag{22}$$

where $D_{i,q}$ is the molecular mass diffusivity of species i in phase q (m^2/s) and $\mathrm{Sc}_t = 0.7$ is the turbulent Schmidt number.

For every reaction, the species source terms are assembled stoichiometrically so that the phase-continuity source terms are consistent with Eq. (21). This consistency is essential when condensed slag species are converted into gas species, e.g., ZnO(slag) → Zn(g), or when solid carbon generates gas.

Population Balance Model: S-Gamma Closure

The Eulerian framework treats the gas phase as a continuum characterized by mean-field quantities (volume fraction, velocity, temperature). However, the tuyere-injected gas disperses into a polydisperse bubble swarm whose size distribution controls both the interfacial area available for heat and mass transfer, and the drag exerted on the continuous phase. Tracking this polydispersity requires a population balance equation (PBE) that is solved in addition to the Eulerian conservation laws [18, 37].

The PBE for the number density function $n(L, \mathbf{x}, t)$ (m^{-4}) (describing the number of bubbles per unit volume of mixture per unit size) is written as

$$\frac{\partial n}{\partial t} + \nabla \cdot \left(\mathbf{v}_g \, n \right) + \frac{\partial}{\partial L} \left(G(L,t) \, n \right) = B(L) - D(L), \tag{23}$$

where L is the bubble equivalent diameter (m), $\mathbf{v}_g$ is the dispersed-phase (gas) velocity, $G(L, t)$ is the rate of change of bubble size due to gas expansion and gas generation (m/s), and B and D are the birth and death rates arising from coalescence and breakup events (m^{-4}/s). In an S-Gamma implementation, the distribution is assumed to follow a log-normal form, and the CFD solver transports its moments rather than resolving $n(L)$ on a full-size grid. A presumed-shape closure of this kind represents one unimodal distribution per transported moment set. It cannot itself return the two-mode spectrum shown in Fig. 11, which is a fitted representation of the injected and reaction-generated gas sources. The parameters of the presumed distribution are reconstructed from the transported moments, enabling the local Sauter mean diameter d_{32} and interfacial area density $a_i = 6\alpha_g / d_{32}$ to be updated consistently with the Eulerian gas holdup. For an ideal-gas bubble, the local diameter-growth rate may be written from $V_b = N_b R T_g / p$ as

$$G(L,t) = \frac{D_g L}{Dt} = \frac{L}{3} \left[\frac{1}{N_b} \frac{D_g N_b}{Dt} + \frac{1}{T_g} \frac{D_g T_g}{Dt} - \frac{1}{p} \frac{D_g p}{Dt} \right], \tag{24}$$

where $D_g/Dt = \partial/\partial t + \mathbf{v}_g \cdot \nabla$ is the gas-phase material derivative and N_b is the number of gas moles in a representative bubble. The first term accounts for gas generation or consumption by reactions and interphase mass transfer, the second term accounts for thermal expansion, and the third term accounts for decompression during bubble rise.

Property-Update Coupling

Radiative heat transfer between the hot free-surface gas, furnace surfaces, and slag surface is included through the gray-gas radiation model.

Because slag composition and temperature evolve during fuming, thermophysical properties (especially viscosity) are updated locally at each CFD time step using the current temperature field and transported oxide mass fractions. Negative oxide mass fractions are clipped to zero and renormalized so that the local sum equals unity before evaluating the viscosity correlation. The viscosity is then bounded and underrelaxed to ensure numerical stability. The coupling strategy for the viscosity update within the overall multiphysics loop is summarized in Algorithm 1.

Algorithm 1 advances the reacting multiphase solution through a sequence of accepted physical time steps. At the beginning of each time step, the phase fractions, velocities, pressure, temperature, slag composition, gas composition, turbulence variables, population-balance variables, and slag viscosity are initialized from the previously converged state. Within each nonlinear iteration, all closures affected by viscosity are recalculated, including interphase drag, turbulence transport, species diffusivity, gas–slag mass transfer, bubble slip, and the breakup and coalescence terms used by the population-balance model. Homogeneous and interfacial reaction rates are then evaluated from the current trial fields, and one stoichiometrically consistent source set is applied to the phase-continuity, momentum, species, population-balance, and energy equations. The hydrodynamic equations are solved first, followed by the population balance, slag- and gas-species transport, and energy equations. All of these equations correspond to the same trial time level, while the previously accepted fields remain fixed in the transient discretization. The viscosity closure is subsequently re-evaluated using the updated temperature and slag composition, allowing the algorithm to measure whether the rheological state is consistent with the newly calculated thermochemical fields.

Algorithm 1 contains both the inner property–hydrodynamics–species–energy iteration at fixed step and the outer control: the adaptive time step and its bounds appear in the requirements, the population-balance update is step (6), and step acceptance or rollback is step (7). The listing, the narrative below, Fig. 3, and the solution sequence described in the section "Model Scope, Computational Configuration, and Assumptions" therefore describe the same procedure in the same order.

The outer time loop advances the coupled flow, species, temperature, reaction, and radiation fields from the current physical time to the prescribed final time using adaptive time stepping and rollback. At the start of each trial step, the current converged solution is stored as a recovery state. The trial time step is restricted so that the calculation does not advance beyond the final simulation time. The flow solver is then executed to update velocity, pressure, phase fraction, and the associated hydrodynamic fields. If this solution fails, the trial step is rejected, the stored fields are restored, and the time step is reduced before the calculation is repeated.

Algorithm 1 CFD-coupled update of slag viscosity using temperature and slag composition

Require: Adaptive time step Δt with bounds $\Delta t_{\min}, \Delta t_{\max}$ and reduction factor $\kappa < 1$
Require: Time step Δt, number of steps N
Require: Slag volume fraction field $\alpha_{\text{slag}}(\mathbf{x})$ and threshold α_{tol}
Require: Temperature field $T(\mathbf{x})$
Require: Slag-phase oxide mass fractions $\mathbf{w}(\mathbf{x}) = \{w_i(\mathbf{x})\}_{i=1}^{K}$ (dimensionless)
Require: Viscosity closure $\mu_{\text{slag}} = f_\mu(T, \mathbf{w})$ (basis and validity range specified)
Require: Under-relaxation $\lambda \in (0, 1]$, bounds $\mu_{\min}, \mu_{\max}$
Require: Inner-iteration limit $m_{\max}$, tolerances $\varepsilon_T, \varepsilon_w, \varepsilon_\mu$
Require: Norm definition $\|\cdot\|_{\Omega_{\text{slag}}}$ over $\Omega_{\text{slag}} = \{\mathbf{x} : \alpha_{\text{slag}} > \alpha_{\text{tol}}\}$

Initialise fields at $t = t_0$: $T^0(\mathbf{x}), \mathbf{w}^0(\mathbf{x}), \mu_{\text{slag}}^0(\mathbf{x})$
for $n = 0$ to $N - 1$ **do**
  Set $T^{(0)} \leftarrow T^n$, $\mathbf{w}^{(0)} \leftarrow \mathbf{w}^n$, $\mu_{\text{slag}}^{(0)} \leftarrow \mu_{\text{slag}}^n$
  for $m = 0$ to $m_{\max} - 1$ **do**
  (1) Property closure (local, slag region only):
    for all $\mathbf{x} \in \Omega_{\text{slag}}$ **do**
      Enforce bounds and normalise composition: $w_i \leftarrow \max(w_i, 0)$; $w_i \leftarrow w_i / \sum_j w_j$
      $\mu^\star(\mathbf{x}) \leftarrow f_\mu\Big(T^{(m)}(\mathbf{x}), \mathbf{w}^{(m)}(\mathbf{x})\Big)$
      $\mu_{\text{slag}}^{(m+1)}(\mathbf{x}) \leftarrow \min\big(\max((1-\lambda)\mu_{\text{slag}}^{(m)}(\mathbf{x}) + \lambda\,\mu^\star(\mathbf{x}), \mu_{\min}), \mu_{\max}\big)$
    end for
    for all $\mathbf{x} \notin \Omega_{\text{slag}}$ **do**
      $\mu_{\text{slag}}^{(m+1)}(\mathbf{x}) \leftarrow \mu_{\text{slag}}^{(m)}(\mathbf{x})$
    end for
  (2) Hydrodynamics:
    Solve continuity + momentum (and turbulence, if used) using $\mu_{\text{slag}}^{(m+1)}$
    $\Rightarrow \mathbf{u}^{(m+1)}(\mathbf{x}), \alpha^{(m+1)}(\mathbf{x})$
  (3) Composition transport + reactions:
    Solve slag composition transport for $\mathbf{w}$ with reaction source terms
    $\Rightarrow \mathbf{w}^{(m+1)}(\mathbf{x})$
  (4) Energy equation:
    Solve energy with heat transfer and reaction enthalpy source $S_h(\mathbf{x})$
    $\Rightarrow T^{(m+1)}(\mathbf{x})$
  (5) Inner convergence (relative):
    $\Delta_T \leftarrow \dfrac{\|T^{(m+1)} - T^{(m)}\|_{\Omega_{\text{slag}}}}{\|T^{(m+1)}\|_{\Omega_{\text{slag}}} + \delta}$
    $\Delta_w \leftarrow \dfrac{\|\mathbf{w}^{(m+1)} - \mathbf{w}^{(m)}\|_{\Omega_{\text{slag}}}}{\|\mathbf{w}^{(m+1)}\|_{\Omega_{\text{slag}}} + \delta}$
    $\Delta_\mu \leftarrow \dfrac{\|\mu_{\text{slag}}^{(m+1)} - \mu_{\text{slag}}^{(m)}\|_{\Omega_{\text{slag}}}}{\|\mu_{\text{slag}}^{(m+1)}\|_{\Omega_{\text{slag}}} + \delta}$
    if $(\Delta_T < \varepsilon_T) \wedge (\Delta_w < \varepsilon_w) \wedge (\Delta_\mu < \varepsilon_\mu)$ **then**
      break
    end if
  end for
  (6) Population balance:
  Advance the transported moments; update d_{32} and $a_i = 6\alpha_g / d_{32}$
  (7) Step acceptance or rollback:
  if converged and global mass, elemental, and energy balances closed **then**
    Accept time step:
    $T^{n+1} \leftarrow T^{(m+1)}$, $\mathbf{w}^{n+1} \leftarrow \mathbf{w}^{(m+1)}$, $\mu_{\text{slag}}^{n+1} \leftarrow \mu_{\text{slag}}^{(m+1)}$
  else
    Restore last accepted state; $\Delta t \leftarrow \max(\kappa\,\Delta t, \Delta t_{\min})$; retry
  end if
end for

After a successful flow solution, the algorithm performs an inner Picard iteration to couple species transport with the slag-energy equation. The species field is first updated using the latest temperature estimate and the newly calculated flow field. The resulting composition is projected onto its physically admissible range so that all mass fractions remain bounded and their sum remains unity. Reaction and radiative source terms are then evaluated at a common linearization state. Their temperature sensitivity is incorporated into the energy equation through implicit and explicit source contributions, which improves numerical stability compared with a fully explicit treatment. The energy equation is subsequently solved to obtain a revised temperature field, and the species and temperature updates are repeated until both fields satisfy their prescribed convergence tolerances or the maximum number of Picard iterations is reached.

A trial step is accepted only when the flow solution succeeds and the coupled species–energy iteration converges. The converged temperature, composition, velocity, pressure, and phase fields are then assigned to the new physical time, after which the simulation proceeds to the next step. If convergence is not achieved, all trial-field modifications are discarded, the previous accepted state is restored, and the time step is multiplied by the specified reduction factor. This rejection-and-retry procedure continues until convergence is obtained or the reduced time step falls below the minimum allowable value, in which case the calculation is terminated. The algorithm therefore combines segregated thermochemical coupling, source-term linearization, adaptive time-step reduction, and complete rollback to prevent an unconverged trial state from contaminating the accepted transient solution.

Acknowledgements The authors gratefully acknowledge Boliden AB and Linde Sverige AB for their collaboration and technical support throughout the ModFurn project. In particular, the authors thank Åke Roos, Business Development, Boliden Smelters, and David Muren, Director of R&D Metals and Combustion EMEA, Global Functions Technology, Linde, for their valuable guidance, continued support, and contributions to the development of the project. The ModFurn project is funded by the Swedish Knowledge Foundation (KKS).

Author Contributions Mehrdad Mesgarpour: Conceptualization, Methodology, Software, Formal analysis, Investigation, Data curation, Writing—original draft, Visualization. Andreas Lennartsson: Investigation, Methodology, Software, Validation, Formal analysis, Writing—review and editing. Magnus Ek: Investigation, Methodology, Validation, Writing—review and editing. Esin İplik: Investigation, Methodology, Validation, Writing—review and editing. Konstantinos G. Kyprianidis: Conceptualization, Methodology, Writing—review and editing. Rebei Bel Fdhila: Supervision, Conceptualization, Methodology, Writing—review and editing.

Funding Open access funding provided by Mälardalen University.

Data Availability The reaction mechanism, thermodynamic data file, and finite-rate kinetic parameters are available based on reasonable request. The population-balance kernel definitions, geometry, post-processing scripts, and the Boliden furnace ZnO and cooling-system data used in Fig. 5c and d are available on reasonable request, the plant data subject to the agreement of Boliden AB.

Conflict of interest The authors declare that they have no known competing financial interests or personal relationships that could have appeared to influence the work reported in this paper.

Declaration of Generative AI and AI-assisted technologies in the writing process During the preparation of this work, the authors used AI-assisted tools to improve the clarity and language of selected sections. The authors subsequently reviewed, revised, and approved the text, and take full responsibility for the content of the publication.

Open Access This article is licensed under a Creative Commons Attribution 4.0 International License, which permits use, sharing, adaptation, distribution and reproduction in any medium or format, as long as you give appropriate credit to the original author(s) and the source, provide a link to the Creative Commons licence, and indicate if changes were made. The images or other third party material in this article are included in the article's Creative Commons licence, unless indicated otherwise in a credit line to the material. If material is not included in the article's Creative Commons licence and your intended use is not permitted by statutory regulation or exceeds the permitted use, you will need to obtain permission directly from the copyright holder. To view a copy of this licence, visit http://creativecommons.org/licenses/by/4.0/.

References

1. Bellemans I, De Wilde E, Moelans N, Verbeken K (2018) Metal losses in pyrometallurgical operations—a review. Adv Coll Interface Sci 255:47–63. https://doi.org/10.1016/j.cis.2017.08.001
2. Klaffenbach E, Montenegro V, Guo M, Blanpain B (2023) Sustainable and comprehensive utilization of copper slag: a review and critical analysis. J Sustain Metall 9:468–496. https://doi.org/10.1007/s40831-023-00683-4
3. Huda N, Naser J, Brooks G, Reuter MA, Matusewicz RW (2012) CFD modeling of Zn slag fuming process in top-submerged lance smelting furnace. Metall Mater Trans B 43(1):39–55. https://doi.org/10.1007/s11663-011-9558-6
4. Richards GG, Brimacombe JK (1985) Kinetics of the zinc slag-fuming process: part II—mathematical model. Metall Trans B 16(3):529–540. https://doi.org/10.1007/BF02654851
5. Cockcroft SL, Richards GG, Brimacombe JK (1989) High-pressure coal injection in zinc slag fuming. Metall Trans B 20(2):227–235. https://doi.org/10.1007/bf02825603
6. Mills KC, Yuan L, Jones RT (2011) Estimating the physical properties of slags. Southern African pyrometallurgy 2011. Johannesburg
7. Mostaghel S, Matsushita T, Samuelsson C, Björkman B, Seetharaman S (2013) Influence of alumina on physical properties of an industrial zinc-copper smelting slag: part 1—Viscosity. Miner Process Extract Metall 122(1):42–48. https://doi.org/10.1179/1743285512Y.0000000032
8. Huda N, Naser J, Brooks GA, Reuter MA, Matusewicz RW (2012) Computational fluid dynamics (CFD) investigation of submerged combustion behavior in a tuyere blown slag-fuming furnace. Metall Mater Trans B 43(5):1054–1068. https://doi.org/10.1007/s11663-012-9686-7
9. Sattar MA, Naser J, Brooks G (2014) Numerical simulation of slag foaming with reaction kinetics in gas injected liquids. Procedia Eng 90:124–129. https://doi.org/10.1016/j.proeng.2014.11.824

10. Obiso D, Schwitalla DH, Korobeinikov I, Meyer B, Reuter MA, Richter A (2020) Dynamics of rising bubbles in a quiescent slag bath with varying thermo-physical properties. Metall Mater Trans B 51(6):2843–2861. https://doi.org/10.1007/s11663-020-01947-0
11. Obiso D, Reuter M, Richter A (2021) CFD investigations of bath dynamics in a pilot-scale TSL furnace. Metall Mater Trans B 52(5):3064–3077. https://doi.org/10.1007/s11663-021-02233-3
12. Cheng Z, Khaliq A, Blanpain B, Guo M (2022) Zn fuming kinetics in a bubble-stirred molten slag bath. Metall Mater Trans B 53(2):1308–1319. https://doi.org/10.1007/s11663-022-02449-x
13. Cheng Z, Khaliq A, Guo M (2022) An updated reactive fraction model to simulate the Zn slag fuming process. Metall Mater Trans B 53(6):3934–3944. https://doi.org/10.1007/s11663-022-02624-0
14. Verscheure K, Van Camp M, Blanpain B, Wollants P, Hayes P, Jak E (2007) Continuous fuming of zinc-bearing residues: part I—model development. Metall Mater Trans B 38(1):13–20. https://doi.org/10.1007/s11663-006-9010-5
15. Verscheure K, Van Camp M, Blanpain B, Wollants P, Hayes P, Jak E (2007) Continuous fuming of zinc-bearing residues: part II–the submerged-plasma zinc-fuming process. Metall Mater Trans B 38(1):21–33. https://doi.org/10.1007/s11663-006-9011-4
16. Khartcyzov G, Shishin D, Ek M, Jak E (2023) The thermodynamic modelling of the Zn slag fuming with the use of coal and ammonia. JOM 75(6):2003–2015. https://doi.org/10.1007/s11837-023-05732-7
17. Guo J, Liu Z, Wang P, Huang X, Li J, Xu K, Zheng C (2015) Numerical investigation on oxy-combustion characteristics of a 200 MWe tangentially fired boiler. Int J Heat Mass Transf 90:218–226. https://doi.org/10.1016/j.ijheatmasstransfer.2015.06.061
18. Lo S, Zhang D (2009) Modelling of break-up and coalescence in bubbly two-phase flows. J Comput Multiph Flows 1(1):23–38. https://doi.org/10.1260/175748209787387106
19. Simcenter STAR-CCM+ User Guide, Version 2406. Siemens Digital Industries Software (2024)
20. Wang J-P, Erdenebold U (2020) A study on reduction of copper smelting slag by carbon for recycling into metal values and cement raw material. Sustainability 12(4):1421. https://doi.org/10.3390/su12041421
21. Ansys Chemkin-Pro Theory Manual, Release 2026 R1 (2026). Ansys, Inc., Canonsburg
22. Hasegawa M, Tanaka T (2000) Viscosity estimation of molten slags. In: Proceedings of the sixth international conference on molten slags, fluxes and salts. CD-ROM proceedings. Stockholm–Helsinki
23. Crowe CT, Sommerfeld M, Tsuji Y (1998) Multiphase flows with droplets and particles. CRC Press, Boca Raton
24. Shih T-H, Liou WW, Shabbir A, Yang Z, Zhu J (1995) A new k-ϵ eddy viscosity model for high Reynolds number turbulent flows. Comput Fluids 24(3):227–238. https://doi.org/10.1016/0045-7930(94)00032-T
25. Sato Y, Sadatomi M, Sekoguchi K (1981) Momentum and heat transfer in two-phase bubble flow–I: theory. Int J Multiph Flow 7(2):167–177. https://doi.org/10.1016/0301-9322(81)90003-3
26. Yeoh GH, Tu J (2019) Computational techniques for multiphase flows. Elsevier
27. Jak E, Hayes PC (2002) Phase equilibria and thermodynamics of zinc fuming slags. Can Metall Quart 41(2):163–174. https://doi.org/10.1179/cmq.2002.41.2.163
28. Nagraj S, Chintinne M, Guo M, Blanpain B (2022) Investigation of bath/freeze lining interface temperature based on the rheology of the slag. JOM 74(1):274–282. https://doi.org/10.1007/s11837-021-05020-2
29. Bellemans I, Zietsman J, Verbeken K (2022) Metal losses in slags: a review on the origin of entrained droplets and freeze-lining considerations. J Sustain Metall 8(1):64–90. https://doi.org/10.1007/s40831-021-00477-6
30. Ishii M, Hibiki T (2011) Thermo-fluid dynamics of two-phase flow, 2nd edn. Springer. https://doi.org/10.1007/978-1-4419-7985-8
31. Calderbank PH, Moo-Young MB (1961) The continuous phase heat and mass-transfer properties of dispersions. Chem Eng Sci 16(1–2):39–54. https://doi.org/10.1016/0009-2509(61)87005-X
32. Clift R, Grace JR, Weber ME (1978) Bubbles, drops, and particles. Academic Press, New York
33. Waladan M, Nilmani M (1995) The effect of injection parameters on slag fuming. Can Metall Quart 34(4):311–318. https://doi.org/10.1179/cmq.1995.34.4.311
34. Han Z, Holappa L (2003) Bubble bursting phenomenon in gas/metal/slag systems. Metall Mater Trans B 34(5):525–532. https://doi.org/10.1007/s11663-003-0020-2
35. Wylock C, Larcy A, Colinet P, Cartage T, Haut B (2011) Direct numerical simulation of the CO_2 transfer from spherical bubbles to the surrounding liquid with chemical reactions. Colloids Surf A 381:130–138. https://doi.org/10.1016/j.colsurfa.2011.03.044
36. Marchisio DL, Fox RO (eds) (2007) Multiphase reacting flows: modelling and simulation, vol 492. CISM Courses and Lectures. Springer, Vienna. https://doi.org/10.1007/978-3-211-72464-4
37. Colombo M, Fairweather M (2016) RANS simulation of bubble coalescence and break-up in bubbly two-phase flows. Chem Eng Sci 146:207–225. https://doi.org/10.1016/j.ces.2016.02.034

Publisher's Note Springer Nature remains neutral with regard to jurisdictional claims in published maps and institutional affiliations.